



1 **Spectral- and size-resolved mass absorption efficiency of mineral dust aerosols in**
2 **the shortwave: a simulation chamber study**

3 Lorenzo Caponi^{1,2}, Paola Formenti¹, Dario Massabò², Claudia Di Biagio¹, Mathieu Cazaunau¹, Edou-
4 ard Panguì¹, Servanne Chevaillier¹, Gautier Landrot³, Meinrat O. Andreae^{4,11}, Konrad Kandler⁵, Stuart
5 Piketh⁶, Thuraya Saeed⁷, Dave Seibert⁸, Earl Williams⁹, Yves Balkanski¹⁰, Paolo Prati², and Jean-
6 François Doussin¹

7 ¹ *Laboratoire Interuniversitaire des Systèmes Atmosphériques (LISA), UMR 7583, CNRS, Université Paris-Est-*
8 *Créteil et Université Paris Diderot, Institut Pierre Simon Laplace, Créteil, France*

9 ² *University of Genoa, Department of Physics & INFN, Genoa, Italy*

10 ³ *Synchrotron SOLEIL, L'Orme des Merisiers Saint-Aubin, France*

11 ⁴ *Biogeochemistry Department, Max Planck Institute for Chemistry, P.O. Box 3060, 55020, Mainz, Germany*

12 ⁵ *Institut für Angewandte Geowissenschaften, Technische Universität Darmstadt, Schnittspahnstr. 9, 64287*
13 *Darmstadt, Germany*

14 ⁶ *Climatology Research Group, University of the Witwatersrand, Johannesburg, South Africa*

15 ⁷ *Science department, College of Basic Education, Public Authority for Applied Education and Training, Al-*
16 *Ardeya, Kuwait*

17 ⁸ *Walden University, Minneapolis, Minnesota, USA*

18 ⁹ *Massachusetts Institute of Technology, Cambridge, Massachusetts, USA*

19 ¹⁰ *LSCE, CNRS UMR 8212, CEA, Université de Versailles Saint-Quentin, Gif sur Yvette, France*

20 ¹¹ *Geology and Geophysics Department, King Saud University, Riyadh, Saudi Arabia*

21
22 * Corresponding author: paola.formenti@lisa.u-pec.fr
23



24 **Abstract**

25 This paper presents new laboratory measurements of the mass absorption efficiency (MAE) between
26 375 and 850 nm for mineral dust of different origin in two size classes: PM_{10.6} (mass fraction of particles
27 of aerodynamic diameter lower than 10.6 μm) and PM_{2.5} (mass fraction of particles of aerodynamic
28 diameter lower than 2.5 μm). Experiments have been performed in the CESAM simulation chamber
29 using generated mineral dust from natural parent soils, and optical and gravimetric analyses.

30 Results show that the MAE values are lower for the PM_{10.6} mass fraction (range 37-135 10⁻³ m² g⁻¹ at
31 375 nm) than for the PM_{2.5} (range 95-711 10⁻³ m² g⁻¹ at 375 nm), and **decrease** with increasing wave-
32 length as λ^{-AAE} , where Angstrom Absorption Exponent (AAE) averages between 3.3-3.5, regardless of
33 size. The size-independence of AAE suggests that, for a given size distribution, the possible variation of
34 dust composition with size would not affect significantly the spectral behavior of shortwave absorption.
35 Because of its high atmospheric concentration, light-absorption by mineral dust can be competitive to
36 black and brown carbon even during atmospheric transport over heavy polluted regions, when dust con-
37 centrations are significantly lower than at emission. The AAE values of mineral dust are higher than for
38 black carbon (~1), but in the same range as light-absorbing organic (brown) carbon. As a result, depend-
39 ing on the environment, there can be some ambiguity in apportioning the AAOD based on spectral de-
40 pendence, which is relevant to the development of remote sensing of light-absorption aerosols from
41 space, and their assimilation in climate models. We suggest that the sample-to-sample variability in our
42 dataset of MAE values is related to regional differences of the mineralogical composition of the parent
43 soils. Particularly in the PM_{2.5} fraction, we found a strong linear correlation between the dust light-
44 absorption properties and elemental iron rather than the iron oxide fraction, which could ease the appli-
45 cation and the validation of climate models that now start to include the representation of the dust com-
46 position, as well as for remote sensing of dust absorption in the UV-VIS spectral region.

47 **1. Introduction**

48 Mineral dust aerosols emitted by wind erosion of arid and semi-arid soils account for about 40% of the
49 total emitted aerosol mass per year at the global scale (Knippertz and Stuut, 2014). The episodic but
50 frequent transport of intense mineral dust plumes is visible from spaceborne sensors as their high con-
51 centrations, combined to their ability of scattering and absorbing solar and thermal radiation, give raise
52 to the highest registered values of aerosol optical depth (AOD) on Earth (Chiapello, 2014). The instan-
53 taneous radiative efficiency of dust particles, that is, their radiative effect per unit AOD, is of the order



54 of tenths to hundreds of $\text{W m}^{-2} \text{AOD}^{-1}$ in the solar spectrum, and of the order of order of tenths W m^{-2}
55 AOD^{-1} in the thermal infrared (e.g., Haywood et al., 2003; di Sarra et al., 2011; Slingo et al., 2006 and
56 the compilation of Highwood and Ryder, 2014). In the solar spectrum, (Boucher et al., 2013). Albeit
57 partially compensated by the radiative effect in the thermal infrared, the global mean radiative effect of
58 mineral dust in the shortwave is negative both at the surface and the top of the atmosphere (TOA) and
59 local warming of the atmosphere. Many are the consequences on the global and regional climate, that
60 ultimately feed back on wind speed and vegetation and therefore on dust emission (Tegen and Lacis,
61 1996; Solmon et al., 2008; Pérez et al., 2006; Miller et al., 2014). Dust particles perturb the surface air
62 temperature through their radiative effect at TOA, can increase the atmospheric stability (e.g., Zhao et
63 al. 2011) and might affect precipitation at the global and regional scale (Solmon et al., 2008; Xian, 2008;
64 Vinoj et al., 2014; Miller et al., 2014 and references therein).

65 All models show that the effect of mineral dust on climate has a great sensitivity to the shortwave ab-
66 sorption properties of mineral dust (Lau et al., 2009; Loeb and Su, 2010; Ming et al., 2010; Perlwitz and
67 Miller, 2010). Absorption by mineral dust started receiving a great deal of interest in the last ten years
68 or so, when spaceborne and ground-based remote sensing studies (Dubovik et al., 2002; Colarco et al.,
69 2002; Sinyuk et al., 2003) suggested that mineral dust was less absorbing that it had been indicated by
70 in situ observations (e.g. Patterson et al., 1977; Haywood et al., 2001), particularly at wavelengths below
71 600 nm. Balkanski et al. (2007) showed that lowering the dust absorption properties to an extent that
72 reconcile them both with the remote-sensing observations and the state-of-knowledge of the mineralog-
73 ical composition, allowed calculating clear-sky dust shortwave radiative effect in agreement with satel-
74 lite-based observations. A significant body of observations have been performed in quantifying the
75 shortwave light-absorbing properties of mineral dust, by direct measurements (Alfaro et al., 2004; Linke
76 et al., 2006; Osborne et al., 2008; McConnell et al., 2008; Derimian et al., 2008; Yang et al., 2009;
77 Müller et al., 2009; Petzold et al., 2009; Formenti et al., 2011; Moosmüller et al., 2012; Wagner et al.,
78 2012; Ryder et al., 2013a; Utry et al., 2015; Denjean et al., 2015c; 2016), and indirectly, by quantifying
79 the amount and the speciation of the light-absorbing compounds in mineral dust, principally iron oxides
80 (Lafon et al., 2004; 2006; Lazaro et al., 2008; Derimian et al., 2008; Zhang et al., 2008; Kandler et al.,
81 2007; 2009; 2011; Formenti et al., 2014a; 2014b).

82 However, existing data are often limited to a single wavelength, which moreover are not identical for all
83 experiments. Also, frequently they do not represent the possible regional variability of the dust absorp-
84 tion, either because they are obtained from field measurements integrating the contributions of different



85 source regions, or conversely, by laboratory investigation targeting samples from a limited number of
86 locations. This might lead to biases. Indeed, iron oxides in mineral dust, mostly in the form of hematite
87 (Fe_2O_3) and goethite ($\text{Fe}(\text{O})\text{OH}$), have specific absorption bands in the UV-VIS spectrum (Bédidi and
88 Cervelle, 1993), and have a variable content depending on the soil mineralogy of the source regions
89 (Journet et al., 2014).

90 Henceforth, in this study we present a new evaluation of the ultraviolet to near-infrared (375-850 nm)
91 light-absorbing properties of mineral dust by studying the size-segregated mass absorption efficiency
92 (MAE, units of $\text{m}^2 \text{g}^{-1}$) and its spectral dependence, largely used in climate models to calculate the direct
93 radiative effect of aerosols. Experiments on twelve aerosol samples generated from natural parent top
94 soils from various source regions worldwide have been conducted with a large atmospheric simulation
95 chamber.

96 2. Instruments and methods

97 At a given wavelength λ , the mass absorption efficiency (MAE, units of $\text{m}^2 \text{g}^{-1}$) is defined as the ratio of
98 the aerosol light-absorption coefficient $b_{\text{abs}}(\lambda)$ (units of m^{-1}) and its mass concentration (in $\mu\text{g m}^{-3}$)

99

$$100 \quad MAE(\lambda) = \frac{b_{\text{abs}}(\lambda)}{\text{Mass Conc}} \quad (1)$$

101

102 MAE values for mineral dust aerosol are expressed in.

103 The spectral dependence of the aerosol absorption coefficient $b_{\text{abs}}(\lambda)$ is described by the power-law
104 relationship

105

$$106 \quad b_{\text{abs}}(\lambda) \sim \lambda^{-AAE} \quad (2)$$

107

108 where the AAE is the Ångström Absorption Exponent, representing the negative slope of $b_{\text{abs}}(\lambda)$ in a
109 log-log plot (Moosmüller et al., 2009)

110



111

$$AAE = - \frac{d \ln(b_{abs}(\lambda))}{d \ln(\lambda)} \quad (3)$$

112

113 2.1. The CESAM simulation chamber

114 Experiments in this work have been performed in the 4.2 m³ stainless-steel CESAM (French acronym
115 for Experimental Multiphase Atmospheric Simulation Chamber) simulation chamber (Wang et al.,
116 2011). The CESAM chamber has been extensively used in recent years to simulate, at sub and super-
117 saturated conditions, the formation and properties of aerosols at concentration levels comparable to those
118 encountered in the atmosphere (Denjean et al., 2015a; 2015b; Bregonzio-Rozier et al., 2015; 2016; Di
119 Biagio et al., 2014; 2016).

120 CESAM is a multi-instrumented platform, equipped with twelve circular flanges to support its analytical
121 environment. Basic instrumentation comprises sensors to measure the temperature, pressure and relative
122 humidity within the chamber (two manometers MKS Baratrons (MKS, 622A and MKS, 626A) and a
123 HMP234 Vaisala® humidity and temperature sensor). The particle size distribution is routinely meas-
124 ured by a combination of (i) a scanning mobility particle sizer (SMPS, mobility diameter range 0.02–
125 0.88 μm), composed of a Differential Mobility Analyzer (DMA, TSI Inc. Model 3080) and a Conden-
126 sation Particle Counter (CPC, TSI Inc. Model 3772); (ii) a SkyGrimm optical particle counter (Grimm
127 Inc., model 1.129, optical equivalent diameter range 0.25–32 μm); and (iii) a WELAS optical particle
128 counter (PALAS, model 2000, optical equivalent diameter range 0.5–47 μm). Full details of operations
129 and data treatment of the particle counters are provided in Di Biagio et al. (2016).

130 2.2. Filter sampling

131 Three filter samples per top soil sample were collected on different types of substrate based on the anal-
132 ysis to perform. Sampling dedicated to the determination of the aerosol mass concentration by gravimet-
133 ric analysis and the measurement of the absorption coefficients by optical analysis was performed on
134 47-mm quartz membranes (Pall Tissuquartz™, 2500 QAT-UP). Two samples were collected in parallel.
135 The first quartz membrane sample (“total”) was collected without a dedicated size cut-off using an in-
136 house built stainless steel sampler operated at 5 L min⁻¹. However, as detailed in Di Biagio et al. (2016),
137 the length of the sampling line from the intake point in the chamber to the filter entrance was 50 cm,
138 yielding with a 50% cut-off of the transmission efficiency at 10.6 μm in particle aerodynamic diameter.
139 This fraction is therefore indicated as PM_{10.6} in the forthcoming discussion. The second quartz membrane



140 sample was collected using a 4-stage DEKATI impactor operated at the flow rate of 10 L min⁻¹ to select
141 the aerosol fraction of particles with aerodynamic diameter smaller than 2.5 μm, indicated as PM_{2.5} here
142 forth. Sampling for the analysis of the iron oxide content was performed on polycarbonate filters (47-
143 mm Nuclepore, Whatman; pore size of 0.4 μm) using the same sample holder than used for the total
144 quartz filters, and therefore referring to the PM_{10.6} mass fraction. Samples were collected at a flow rate
145 of 6 L min⁻¹. All flow rates were monitored by a thermal mass flow meter (TSI Inc., model 4140). These
146 samples were also used to determine the elemental composition (including Fe) and the fraction of iron
147 oxides in the total mass.

148 **2.3. The Multi-Wavelength Absorbance Analyzer (MWAA)**

149 The aerosol absorption coefficient $b_{\text{abs}}(\lambda)$ at 5 wavelengths ($\lambda = 375, 407, 532, 635$ and 850 nm) was
150 measured by *in situ* analysis of the quartz filter samples using the Multi-Wavelength Absorbance Ana-
151 lyzer (MWAA), described in detail in Massabò et al. (2013; 2015).

152 The MWAA performs a non-destructive scan of the quartz filters on 64 different points, each ~ 1 mm²
153 wide. It measures the light transmission through the filter as well as backscattering at two different angles
154 (125° and 165°). This is necessary to constrain the multiple scattering effects occurring within the par-
155 ticle-filter system. Measurements are used as input of a radiative transfer model (Hänel, 1987; 1994) as
156 implemented by Petzold and Schölinner (2004) for the Multi-Angle Absorption Photometry (MAAP)
157 measurements. In this model, a two stream approximation is applied (Coakley and Chylek, 1975), in
158 which the fractions of hemispherical backscattered radiation with respect to the total scattering for col-
159 limated and diffuse incident radiation are approximated on the basis of the Henyey-Greenstein scattering
160 phase function (Hänel, 1987). This approximation assumes a wavelength-independent asymmetry pa-
161 rameter (g) set to 0.75, appropriate for mineral dust (Formenti et al., 2011; Ryder et al., 2013b). The
162 total uncertainty, including the effects of photon counting and the deposit inhomogeneity, on the absorp-
163 tion coefficient measurement is estimated at 8%.

164 **2.4. Gravimetric analysis**

165 The aerosol mass deposited on filter (μg) was obtained by weighing the quartz filter before and after
166 sampling, after a period of 48 hours of conditioning in a room with controlled atmospheric conditions
167 (temperature, $T \sim 20 \pm 1$ °C; relative humidity, $RH \sim 50 \pm 5\%$). Weighting is performed with an analyt-
168 ical balance (Sartorius model MC5, precision of 1 μg), and repeated three times to control the statistical
169 variability of the measurement. Electrostatic effects are removed by exposing the filters, prior weighing,



170 to a de-ionizer. The error on the measured mass is estimated at 10 μg , including the repetition variability.
171 The aerosol mass concentration ($\mu\text{g m}^{-3}$) is obtained by dividing the mass deposited on filter to the total
172 volume of sampled air (m^3) obtained from the mass flowmeter measurements.

173 **2.5. Dust composition measurements**

174 **2.5.1. Elemental composition**

175 Elemental concentrations for the major constituents of mineral dust (Na, Mg, Al, Si, P, S, Cl, K, Ca, Fe,
176 Ti, Mn) were obtained by a Wavelength Dispersive X-ray fluorescence (WD-XRF) of the Nuclepore
177 filters using a PW-2404 spectrometer by Panalytical. Excitation X-rays are produced by a Coolidge tube
178 ($I_{\text{max}} = 125 \text{ mA}$, $V_{\text{max}} = 60 \text{ kV}$) with a Rh anode; primary X-ray spectrum can be controlled by inserting
179 filters (Al, at different thickness) between the anode and the sample. Each element was analyzed three
180 times, with specific conditions (voltage, tube filter, collimator, analyzing crystal and detector). Data
181 collection was controlled by the SuperQ software provided with the instrument. The elemental mass
182 thickness ($\mu\text{g cm}^{-2}$), that is, the analyzed elemental mass per unit surface, was obtained by comparing
183 the elemental yields with a sensitivity curve measured in the same geometry on a set of certified mono-
184 or bi-elemental thin layer standards by Micromatter Inc. The certified uncertainty on the standard deposit
185 ($\pm 5\%$) determines the lower limit on the uncertainty on the measured elemental concentrations, which
186 range between 8% and 10% depending on the considered element. Thanks to the uniformity of the aer-
187 osol deposit on the filters, the atmospheric elemental concentrations ($\mu\text{g m}^{-3}$) were calculated by multi-
188 plying the analyzed elemental mass thickness by the ratio between the collection and analyzed surfaces
189 of each sample (41 and 22 mm, respectively), then divided by the total sampled volume (m^3). Finally,
190 concentrations of light-weight elements (atomic number $Z < 19$) were corrected for the underestimation
191 induced by the self-absorption of the emitted soft X-rays inside aerosol particles according to Formenti
192 et al. (2011).

193 Additional XRF analysis of the quartz filters has been performed both in the $\text{PM}_{10.6}$ and the $\text{PM}_{2.5}$ frac-
194 tions, so to verify the absence of biases between the experiments dedicated to the determination of par-
195 ticle composition to those where the optical properties were measured.

196 **2.6.2. Iron oxide content**

197 The content and the mineralogical speciation of iron oxides, also defined as free-iron, that is, the fraction
198 of iron which is not in the crystal lattice of silicates (Karickhoff and Bailey, 1973), was determined by



199 XANES (X-ray absorption near-edge structure) in the Fe K-range (K_{α} , 7112 eV) at the SAMBA (Spec-
200 troscopies Applied to Materials based on Absorption) beamline at the SOLEIL synchrotron facility in
201 Saclay, France (Briois et al., 2011). The position and shape of the K pre-edge and edge peaks were
202 analyzed as they depend on the oxidation state of iron and the atomic positions of the neighboring ions,
203 mostly O^+ and OH^- .

204 As in Formenti et al. (2014b), samples were mounted in an external setup mode. A Si(220) double-
205 crystal monochromator was used to produce a monochromatic X-ray beam, which was $3000 \times 250 \mu\text{m}^2$
206 in size at focal point. The energy range was scanned from 6850 eV to 7800 eV at a step resolution
207 varying between 0.2 eV in proximity to the Fe-K absorption edge (at 7112 eV) to 2 eV in the extended
208 range. Samples were analyzed in fluorescence mode without prior preparation. One scan acquisition
209 lasted approximately 30 minutes, and was repeated three times to improve the signal-to-noise ratio.

210 The same analytical protocol was applied to five standards of Fe(III)-bearing minerals (**Table 1**), includ-
211 ing iron oxides (hematite, goethite) and silicates (illite, montmorillonite, nontronite). The standard spec-
212 tra were used to deconvolute the dust sample spectra to quantify the mineralogical status of iron. The
213 linear deconvolution, performed the Athena IFEFFIT freeware analysis program (Ravel and Newville,
214 2005), provided with the proportionality factors α_i representing the mass fraction of elemental iron to be
215 assigned to the i -th standard mineral. In particular, the values of α_{hem} and α_{goe} represent the mass frac-
216 tions of elemental iron that can be attributed to hematite and goethite, and $\alpha_{Fe\text{ ox}}$ ($\alpha_{hem} + \alpha_{goe}$), the mass
217 fraction of elemental iron that can be attributed to iron oxides.

218 **2.6.3. Calculation of the iron oxide content**

219 The measured elemental concentrations obtained by X-ray fluorescence are expressed in the form of
220 elemental oxides and summed to estimate the total mineral dust mass concentration MC_{dust} according to
221 the equation from Lide (1992)

222

$$223 \quad [MC_{dust}] = 1.12 \times \left\{ \begin{array}{l} 1.658[Mg] + 1.889[Al] + 2.139[Si] + 1.399[Ca] + 1.668[Ti] + 1.582[Mn] \\ + (0.5 \times 1.286 + 0.5 \times 1.429 + 0.47 \times 1.204)[Fe] \end{array} \right\} \quad (4)$$

224

225 The relative uncertainty on MC_{dust} , estimated from the analytical error on the measured concentrations,
226 does not exceed 6%.



227 The fractional mass ratio (in percent) of elemental iron ($MR_{Fe\%}$) with respect to the total dust mass con-
 228 centration MC_{dust} is then calculated as

229

$$230 \quad MR_{Fe\%} = \frac{[Fe]}{[MC_{Dust}]} \times 100 \quad (5)$$

231

232 The mass concentration of iron oxides or free-iron ($MC_{Fe\ ox}$), representing the fraction of elemental iron
 233 in the form of hematite and goethite (Fe_2O_3 and $FeOOH$, respectively), is equal to

234

$$235 \quad MC_{Fe\ ox} = MC_{hem} + MC_{goe} \quad (6)$$

236

237 where MC_{hem} and MC_{goe} are the total masses of hematite and goethite. These can be calculated from the
 238 values α_{hem} and α_{goe} from XANES analysis, which represent the mass fractions of elemental iron at-
 239 tributed to hematite and goethite, as

240

$$241 \quad MC_{hem} = \frac{\alpha_{hem} \times [Fe]}{0.70} \quad (7.a)$$

$$242 \quad MC_{goe} = \frac{\alpha_{goe} \times [Fe]}{0.63} \quad (7.b)$$

243

244 where the values of 0.70 and 0.63 represent the mass molar fractions of Fe in hematite and goethite,
 245 respectively. The relative errors on MC_{hem} and MC_{goe} are obtained from the uncertainties on values α_{hem}
 246 and α_{goe} from XANES analysis (less than 10%).

247 The mass ratio of iron oxides ($MR_{Fe\ ox\%}$) with respect to the total dust mass can then be calculated as

248

$$249 \quad MR_{Fe\ ox\%} = MC_{Fe\ ox} \times MR_{Fe\%} \quad (8)$$

250

251



252 3. Experimental protocol

253 At the beginning of each experiment, the chamber was evacuated by to 10^{-4} - 10^{-5} hPa. Then, the reactor
254 was filled with a mixture of 80% N₂ and 20% O₂ at a pressure slightly exceeding the current atmospheric
255 pressure, in order to avoid contamination from ambient air. Experiments were conducted at ambient
256 temperature and at a relative humidity <2%. As in Di Biagio et al. (2014; 2016), dust aerosols were
257 generated by mechanical shaking of the soils, previously sieved to < 1000 μm and dried at 100 °C for
258 about 1 h to remove any residual humidity. About 15 g of soil was placed in a Buchner flask and shaken
259 for about 30 min at 100 Hz by means of a sieve shaker (Retsch AS200). The dust particles produced was
260 then injected in the chamber by flushing the flask with N₂ at 10 L min⁻¹ for about 10-15 min, whilst
261 continuing shaking the soil.

262 Dust was injected for about 10-15 minutes, and left suspended in the chamber for approximately 120
263 min thanks to the 4-wheel fan located in the bottom of the chamber body. Previous measurements at the
264 top and bottom of the chamber showed that the fan ensures a homogeneous distribution of the dust
265 starting approximately 10 minutes after the end of the injection (Di Biagio et al., 2014).

266 To compensate for the air extracted from the chamber by sampling, a particle-free flow of N₂/O₂, regu-
267 lated in real time as a function of the total volume of sampled air, was re-injected in the chamber. To
268 avoid excessive dilution the flow was limited to 20 L min⁻¹. Two experiments per soil type were con-
269 ducted: a first experiment for sampling on the nuclepore polycarbonate filters (determination of the ele-
270 mental composition and the iron oxide fraction) and *in situ* measurements of the infrared optical con-
271 stants (Di Biagio et al., 2016), and a second experiment on total quartz filter and impactor for the study
272 of dust MAE presented in this paper.

273 **Figure 1** illustrates as typical example the time series of the aerosol mass concentration during the two
274 experiments conducted for the Libyan sample. The comparison demonstrates the repeatability of the dust
275 concentrations, both in absolute values and in temporal dynamics. It also shows that the mass concen-
276 trations decreased very rapidly by gravitational settling within the first 30 minutes of the experiment
277 (see also the discussion in Di Biagio et al. (2016)), after which concentrations only decrease by dilution.
278 The filter sampling was started after this transient phase, and then continued through the end of the
279 experiments, in order to collect enough dust on filter for the chemical analysis. Blank samples were
280 collected before the start of the experiments by placing the loaded filter holders in line with the chamber
281 and by flushing them for a few seconds with air coming from the chamber.



282 At the end of each experimental series with a given soil sample, the chamber was manually cleaned in
283 order to remove carry-over caused by resuspension of particles deposited to the walls. Background con-
284 centrations of aerosols in the chamber vary between 0.5 and 2.0 $\mu\text{g m}^{-3}$, i.e. a factor of 500 to 1000 below
285 the operating conditions.

286 3. Results and discussion

287 The geographical location of the soil collection sites is shown in **Figure 2**, whereas the coordinates are
288 summarized in **Table 2**. As discussed in Di Biagio et al. (2016), the selection of these soils and sediments
289 was governed by the need of representing the major arid and semi-arid regions worldwide, the need of
290 taking into account the mineralogical diversity of the soil composition at the global scale, and finally by
291 their availability in sufficient quantities for injection in the chamber. When doing so, we obtained a set
292 of twelve samples distributed worldwide but mostly in Northern and Western Africa (Libya, Algeria,
293 Mali, Bodélé) and the Middle East (Saudi Arabia and Kuwait). Individual samples from the Gobi desert
294 in Eastern Asia, the Namib Desert, the Strzelecki desert in Australia, the Patagonian deserts in South
295 America, and the Sonoran Desert in Arizona have also been investigated.

296 3.1. Elemental composition and iron oxide content

297 A total of 41 filters including 15 polycarbonate filters (12 samples and 3 blanks) and 25 quartz filters
298 (12 for the total fraction, 10 for the fine fraction and 3 blanks) were collected for analysis.

299 The dust mass concentration found by gravimetric analysis varied between 50 $\mu\text{g m}^{-3}$ and 5 mg m^{-3} , in
300 relatively good agreement with the dust mass concentration MC_{dust} (Equation 4) based on X-ray fluores-
301 cence analysis: the slope of the linear regression between the calculated and the gravimetric values of
302 MC_{dust} is 0.90 with $R^2 = 0.86$.

303 Di Biagio et al. (2016) show that clays are the most abundant mineral phases, together with quartz and
304 calcite, and that significant variability exists as function of the compositional heterogeneity of the parent
305 soils. Here we use the Fe/Ca and Si/Al elemental ratios obtained from X-ray Fluorescence analysis to
306 discriminate the origin of used dust samples. These ratios have been extensively used in the past to
307 discriminate the origin of African dust samples collected in the field (Chiapello et al., 1997; Formenti et
308 al., 2011; Formenti et al., 2014a). The values obtained during our experiments are reported in **Table 3**.
309 There is a very good correspondence between the values obtained for the Mali, Libya, Mauritania and
310 (to a lesser extent) Morocco experiments to values found in environmental aerosol samples. The only



311 major difference is observed for the Bodélé experiment, for which the Fe/Ca ratio is enriched by a factor
312 of 6 with respect to the field observations (Formenti et al., 2011; Formenti et al., 2014a). This could
313 reflect the fact that the Bodélé aerosol in the chamber is generated from a sediment sample and not from
314 a soil. As a matter of fact, the Bodélé sediment sample is constituted by a very fine powder which be-
315 comes very easily airborne. Henceforth, and contrary to the soil samples, this powder is likely to be
316 injected in the chamber with little or no size fractionation. As a consequence, the composition of the
317 aerosol collected in the chamber could reflect more that of the parent sedimentary soil than not the other
318 samples. On the other hand, Bristow et al. (2010) and Moskowitz et al. (2016) show that the iron content
319 and speciation of the Bodélé sediments is very heterogeneous at the source scale. For non-northern Af-
320 rican samples, the largest variability is observed for the Fe/Ca values, ranging from 0.1 to 8, whereas
321 the Si/Al ratio varied between 2.5 and 4.8. In this case, values are available in the literature for compar-
322 ison (e.g., Cornille et al., 1990; Reid et al., 1994; Eltayeb et al., 2001; Lafon et al., 2006; Shen et al.,
323 2007; Radhi et al., 2010; 2011; Formenti et al., 2011; 2014a; Scheuven et al., 2013 and references
324 within). Values in the PM_{2.5} fraction are very consistent with those obtained in the PM_{10.6}: their linear
325 correlation has a slope of 1.03 (± 0.05) and a R^2 equal to 0.97, suggesting that the elemental composition
326 is relatively size-independent.

327 The mass fraction of total Fe ($MC_{Fe\%}$ from Equation 5), also reported in **Table 3**, ranged from 2.8 to
328 7.3%, values found for the Namibia and the Australia samples, respectively. This range is in good agree-
329 ment with values reported in the literature, taking into account that differences might be also due to the
330 method (direct measurement/calculation) and/or the size fraction over which the total dust mass concen-
331 tration is estimated (Chiapello et al., 1997; Reid et al., 1994; 2003; Derimian et al., 2008; Formenti et
332 al., 2001; 2011; 2014a; Scheuven et al., 2013). The agreement of $MC_{Fe\%}$ values obtained by the XRF
333 analysis of polycarbonate filters (Equation 5) and those obtained from the XRF analysis of the quartz
334 filters, normalized to the measured gravimetric mass is well within 10% (that is, the percent error of
335 each estimate). An the exception are the samples of Bodélé and Algeria, for which the values obtained
336 from the analysis of the quartz filters are significantly lower than those obtained from the nuclepore
337 filters. We treat that as an additional source of error in the rest of the analysis, and add it to the total
338 uncertainty. In the PM_{2.5}, the content of iron is more variable, ranging from 4.4% (Morocco) to 33.6%
339 (Mali), showing a size dependence. A word of caution on this conclusion as the two estimates are not
340 necessarily consistent in the way that the total dust mass is estimated (from Equation 4 for the PM_{10.6}
341 fraction and by gravimetric weighing on the PM_{2.5}).



342 Finally, between 11 and 47% of iron in the samples can be attributed to iron oxides, in variable propor-
343 tions between hematite and goethite. The iron oxide fraction of total Fe in this study is on the lower end
344 of the range (36-72%) estimated for field dust samples of Saharan/Sahelian origin (Formenti et al.
345 2014b). The highest value of Formenti et al. (2014b), obtained for a sample of locally-emitted dust col-
346 lected at the Banizoumbou station in the African Sahel, is anyhow in excellent agreement with the value
347 of 62% obtained for an experiment (not shown here) using a soil collected in the same area. Likewise,
348 the proportions between hematite and goethite (not shown) are reproduced, showing that goethite is more
349 abundant than hematite. The mass fraction of iron oxides ($MR_{Fe\ ox\%}$), estimated from Equation 8 and
350 shown in Table 3, ranges between 0.7% (Kuwait) to 3.6% (Australia), which is in the range of available
351 field estimates (Formenti et al., 2014a; Moskowitz et al., 2016). For China, our value of $MR_{Fe\ ox\%}$ is
352 lower by almost a factor of 3 in comparison with that obtained on the same dust sample by Alfaro et al.
353 (2004) (0.9% against 2.8%), whereas on a sample from Niger (however not considered in this study) our
354 estimates and that by Alfaro et al. (2004) perfectly agree (5.8%). A possible underestimate of the iron
355 oxide fraction for samples other than those from the Sahara-Sahel area could be due to the fact that -
356 opposite to the experience of Formenti et al. (2014b) - the linear deconvolutions of the XANES spectra
357 were not always satisfactory (see Figure S1 in the supplementary). This resulted in a significant residual
358 between the observed and fitted XANES spectra. Indeed, the mineralogical reference for hematite is
359 obtained from a soil from Niger (Table 1) and might not be fully suitable for representing aerosols of
360 different origins. Additional differences could arise from differences in the size distributions of the gener-
361 ated aerosol. As a matter of fact, the number fraction of particles in the size classes above 0.5 μm in
362 diameter are different in the dust aerosol generated in the Alfaro et al. (2004) study with respect to ours.
363 In the study by Alfaro et al. (2004), the number fraction is lowest in the 0.5-0.7 size class and highest
364 between 1 and 5 μm . On the contrary, in our study the number fraction is lowest in the 1-2 μm size range
365 and highest between 0.5 and 0.7 μm . These differences could yield either to difference in the chemical
366 composition and/or to a difference in the total mass in the denominator of Equation 8.

367 3.2. Spectral and size-variability of the mass absorption efficiency

368 The spectral mass absorption efficiency (MAE) at 375, 407, 532, 635 and 850 nm for the $\text{PM}_{10.6}$ and the
369 $\text{PM}_{2.5}$ dust fractions are summarized in **Table 4** and displayed in **Figure 3**. Regardless of particle size,
370 the MAE values decrease with increasing wavelength (almost one order of magnitude between 375 and
371 850 nm), and display a larger variability at shorter wavelengths. The MAE values for the $\text{PM}_{10.6}$ range
372 from $37 (\pm 3) 10^{-3} \text{ m}^2 \text{ g}^{-1}$ to $135 (\pm 11) 10^{-3} \text{ m}^2 \text{ g}^{-1}$ at 375 nm, and from $1.3 (\pm 0.1) 10^{-3} \text{ m}^2 \text{ g}^{-1}$ to $15 (\pm 1)$



373 $10^{-3} \text{ m}^2 \text{ g}^{-1}$ at 850 nm. Maxima are found for the Australia and Algeria samples, whereas the minima are
374 for Bodelé and Namibia, respectively at 375 and 850 nm. In the $\text{PM}_{2.5}$ fraction, the MAE values range
375 from $95 (\pm 8) 10^{-3} \text{ m}^2 \text{ g}^{-1}$ to $711 (\pm 70) 10^{-3} \text{ m}^2 \text{ g}^{-1}$ at 375 nm, and from $3.2 (\pm 0.3) 10^{-3} \text{ m}^2 \text{ g}^{-1}$ to $36 (\pm 3)$
376 $10^{-3} \text{ m}^2 \text{ g}^{-1}$ at 850 nm. Maxima at both 375 and 850 nm are found for the Morocco sample, whereas the
377 minima are for Algeria and Namibia, respectively. The MAE values for mineral dust resulting from this
378 work are in relative good agreement with the estimates available in literature (Alfaro et al., 2004; Linke
379 et al., 2006; Yang et al., 2009; Denjean et al., 2016), reported in **Table 5**. For the China Ulah Buhn
380 sample, Alfaro et al. (2004) reported $69.1 10^{-3}$ and $9.8 10^{-3} \text{ m}^2 \text{ g}^{-1}$ at 325 and 660 nm, respectively. The
381 former is lower than the value of $99 10^{-3} \text{ m}^2 \text{ g}^{-1}$ that we obtain by extrapolating our measurement at 375
382 nm. Likewise, our values for the Morocco sample are higher than reported by Linke et al. (2006) at 266
383 and 660 nm. Conversely, the agreement with the estimates of Yang et al. (2009) for mineral dust locally
384 re-suspended in Xianghe, near Beijing (China) is very good at all wavelengths between 375 and 880 nm.
385 As expected, the MAE values for mineral dust resulting from this work are almost one order of magni-
386 tude smaller than for other absorbing aerosols. For black carbon, MAE values are in the range of 6.5–
387 $7.5 \text{ m}^2 \text{ g}^{-1}$ at 850 nm (Bond and Bergstrom, 2006; Massabò et al., 2016), and vary in a linear way in-
388 versely with wavelength. For brown carbon, the reported MAE range between $2.3\text{--}7.0 \text{ m}^2 \text{ g}^{-1}$ at 350 nm
389 (Chen and Bond, 2010; Kirchstetter et al., 2004; Massabò et al., 2016), $0.05\text{--}1.2 \text{ m}^2 \text{ g}^{-1}$ at 440 nm (Wang
390 et al., 2016) and $0.08\text{--}0.72 \text{ m}^2 \text{ g}^{-1}$ at 550 nm (Chen and Bond, 2010).

391 The analysis of **Table 4** indicates that, at every wavelength, the MAE values in the $\text{PM}_{2.5}$ fraction are
392 equal or higher than those for $\text{PM}_{10.6}$. The $\text{PM}_{2.5}/\text{PM}_{10.6}$ MAE ratios reach values of 6 for the Mali sam-
393 ple, but are mostly in the range 1.5–3 for the remaining aerosols. Values decrease with wavelength up to
394 635 nm, whereas at 850 nm they have values comparable to those at 375 nm. The observed size-depend-
395 ence of the MAE values is consistent with the expected behavior of light absorption of particles in the
396 Mie and geometric optical regimes that concern the two size fractions. Light-absorption of particles of
397 size smaller or equivalent to wavelength is proportional to their bulk volume, whereas for larger particles
398 absorption occurs on their surface only (Bohren and Huffman, 1983). On the other hand, the size-
399 resolved measurements of Lafon et al. (2006) show that the proportion (by volume) of iron oxides might
400 be higher in the coarse than in the fine fraction, which would counteract the size-dependence behavior
401 of MAE. To validate the observations, we calculated the spectrally-resolved MAE values in the two size
402 fractions using the Mie code for homogeneous spherical particles (Bohren and Huffman, 1983) and the
403 number size distribution estimated by (Di Biagio et al., 2016) and averaged over the duration of filter



404 sampling. We estimated the dust complex refractive index as a volume-weighted average of a non-ab-
405 sorbing dust fraction having the refractive index of kaolinite, dominant mineral in our samples (see Di
406 Biagio et al., 2016), from Egan et Hilgeman (1979) and an absorbing fraction estimated from the mass
407 fraction of iron oxides and having the refractive index of hematite (Bedidi and Cervelle, 1993). Results
408 of this calculation indicate that the observed size-behavior is well reproduced at all wavelengths, even
409 in the basic hypothesis that the mineralogical composition does not change with size. The only exception
410 is 850 nm, where at times, $PM_{2.5}/PM_{10.6}$ MAE ratio is much higher than expected theoretically. We
411 attribute that to the relatively high uncertainty affecting the absorbance measurements at this wavelength
412 where the signal-to-noise ratio is low. Indeed, the two sets of values (MAE in the $PM_{2.5}$ fraction and
413 MAE in the $PM_{10.6}$ fraction) are not statistically different according to a two-pair t-test (0.01 and 0.05
414 level of confidence), confirming that any attempt of differentiation the size-dependence at this wave-
415 length would require a stronger optical signal.

416 The analysis of the spectral dependence, using a power-law function fit as from Equation 2, provides
417 with the values of the Angstrom Absorption Exponent (AAE), also reported in **Table 4**. Contrary to the
418 MAE values, there is no statistically significant size-dependence of the AAE values, ranging from 2.5
419 (± 0.2) to 4.1 (± 0.3), with an average of 3.3 (± 0.7), for the $PM_{10.6}$ size fraction and between 2.6 (± 0.2)
420 and 5.1 (± 0.4), with an average of 3.5 (± 0.8), for the $PM_{2.5}$ fraction. Our values are in the range of those
421 published in the open literature (Fialho et al., 2005; Linke et al., 2006; Müller et al., 2009; Petzold et al.,
422 2009; Yang et al., 2009; Weinzierl et al., 2011; Moosmüller et al., 2012; Denjean et al., 2016), shown in
423 **Table 5**. AAE values close to 1.0 are found for urban aerosols where fossil fuels combustion is dominant,
424 while AAE values for brown carbon (BrC) from incomplete combustion are in the range 3.5-4.2 (Yang
425 et al., 2009; Chen et al., 2015; Massabò et al., 2016).

426 Finally, **Figure 4** shows correlations between MAE values in the $PM_{10.6}$ fraction (Figure 3.a) and in the
427 $PM_{2.5}$ fraction (Figure 3.b) and the estimated percent mass fraction of iron and iron oxides ($MC_{Fe\%}$ and
428 $MC_{Fe\ ox\%}$), respectively. Regardless of the size fraction, the correlation between the MAE values and the
429 percent mass of total elemental iron are satisfactory. Higher correlations are obtained at 375, 407 and
430 532 nm, and in the $PM_{2.5}$ fraction, where a linear correlation with R^2 up to 0.94 are obtained. Best cor-
431 relations are obtained when forcing the intercept to zero, indicating that elemental iron fully accounts
432 for the measured absorption. At these wavelengths, linear correlations with the mass fraction of iron
433 oxides are loose in the $PM_{10.6}$ mass fraction (R^2 up to 0.38-0.62), but again satisfactory in the $PM_{2.5}$
434 fraction (R^2 up to 0.83-0.99), where, whoever, one should keep in mind that they have been established



435 only indirectly by considering the ratio of iron oxides to elemental iron independent of size. At 660 and
436 850 nm, little or no robust correlation is obtained, often on very few data points and with very low MAE
437 values. It is noteworthy that, in both size fractions, the linear correlation yields a non-zero intercept is
438 obtained, indicating other minerals but iron oxides account for the measured absorption.

439 4. Conclusive remarks

440 In this paper, we reported new laboratory measurements of the shortwave mass absorption efficiency
441 (MAE) of mineral dust of different origin and as a function of size and wavelength in the 375-850 nm
442 range. Results have been obtained in the CESAM simulation chamber using generated mineral dust from
443 natural parent soils, and optical and gravimetric analysis on extracted samples.

444 Our results can be summarized as follows: at 375 nm, the MAE values are lower for the $PM_{10.6}$ mass
445 fraction (range 37-135 $10^{-3} \text{ m}^2 \text{ g}^{-1}$) than for the $PM_{2.5}$ (range 95-711 $10^{-3} \text{ m}^2 \text{ g}^{-1}$), and vary opposite to
446 wavelength as λ^{-AAE} , where AAE (Angstrom Absorption Exponent) averages between 3.3-3.5 regardless
447 of size fraction. These results deserve some conclusive comments:

- 448 • The size-dependence, yielding significantly higher MAE values in the fine fraction ($PM_{2.5}$) than
449 for the $PM_{10.6}$ aerosol, indicates that light-absorption by mineral dust can be important even dur-
450 ing atmospheric transport over heavy polluted regions, when dust concentrations are significantly
451 lower than at emission. This can be shown by comparing the aerosol absorption optical depth
452 (AAOD) at 440 nm for China, a well-known mixing region of mineral dust and pollution (e.g.,
453 Yang et al., 2009; Laskin et al., 2014; Wang et al., 2013). Laskin et al. (2014) reports that the
454 average AAOD in the area is of the order of 0.1, for carbonaceous absorbing aerosols (sum of
455 black and brown carbon). This is lower or comparable to the AAOD of 0.17 and 0.11 at 407 nm
456 (fine and total mass fractions, respectively) that we obtain by a simple calculation (AAOD =
457 MAE \times MC_{dust} \times H), where MAE are the values estimated in this study, MC the dust mass con-
458 centrations typically observed in the area during dust storms (Sun et al., 2001), and H a scale
459 height factor of 1 km.
- 460 • The spectral variability of the dust MAE values, represented by the AAE parameter, is equal in
461 the $PM_{2.5}$ and $PM_{10.6}$ mass fractions. This suggests that, for a given size distribution, the possible
462 variation of dust composition with size do not affect in a significant way the spectral behavior of
463 the absorption properties. Our average value for AAE is 3.3 ± 0.7 , higher than for black carbon,
464 but in the same range than light-absorbing organic (brown) carbon. As a result, depending on the



465 environment, there can be some ambiguity in apportioning the AAOD based on spectral depend-
466 ence. Bahadur et al. (2012) and Chung et al. (2012) couple the AAE and the spectral dependence
467 of the total AOD and/or its scattering fraction only to overcome this problem. Still, Bahadur et
468 al. (2012) show that there is an overlap in the scatterplots of the spectral dependence of the scatter-
469 ing and absorption fractions of the AOD based on analysis of ground-based remote sensing
470 data for mineral dust, urban and non-urban fossil fuel over California. A closer look to observa-
471 tions in mixing areas where biomass burning have different chemical composition and/or mineral
472 dust has heavy loadings should be given in order to generalize the clear separation observed in
473 the spectral dependences of mineral dust and biomass burning (Bahadur et al., 2012). This aspect
474 is relevant to the development of remote sensing of light-absorption aerosols from space, and
475 their assimilation in climate models (Torres et al., 2007; Buchard et al., 2015; Hammer et al.,
476 2016).

477 • There is an important sample-to-sample variability in our dataset of MAE values for mineral dust
478 aerosols. At 532 nm, our estimated MAE average at $34 \pm 14 \text{ m}^2 \text{ g}^{-1}$ and $78 \pm 70 \text{ m}^2 \text{ g}^{-1}$ in the
479 $\text{PM}_{10.6}$ and $\text{PM}_{2.5}$ mass fractions, respectively. Figure 3, showing the correlation with the esti-
480 mated mass fraction of elemental iron and iron oxides, suggests that this variability could be
481 related to the regional differences of the mineralogical composition of the parent soils. These
482 observations lead to different considerations. To start with, our study reinforces the need for
483 regionally-resolved representation of the light-absorption properties of mineral dust in order to
484 improve the representation of its effect on climate. As a matter of fact, the natural variability of
485 the absorption properties that we obtain from our study is in the range 50-100%, even when we
486 limit ourselves to smaller spatial scales, for example those of north Africa (samples from Libya,
487 Algeria, Mali and Bodélé). This is far above the $\pm 5\%$ sensitivity factor used by Solmon et al.
488 (2008) to vary the single scattering albedo (as a proxy of absorption) of mineral dust over western
489 Africa, and to show how this could drastically change the climate response in the region.

490 The question is then “how to represent this regional variability?” As Moosmüller et al. (2012),
491 we found that elemental iron is a very good proxy for the MAE, especially in the $\text{PM}_{2.5}$ fraction,
492 where iron-bearing absorbing minerals (hematite, goethite, illite, smectite clays) would be more
493 concentrated. In the coarse fraction, Ca-rich minerals, quartz and feldspars could also play a role,
494 and that could result in the observed lowered correlation (although adding a term proportional to
495 elemental Ca does not ameliorate the result in the present study). The correlation of the spectral



496 MAE values with the iron oxide fraction is satisfactory but rather noisy, also owing to some
497 uncertainty in the quantification of iron oxides from X-Ray Absorption measurements. In this
498 case, the intercept is significantly different from zero, again indicating that a small but clear
499 fraction of absorption is due to minerals other than iron oxides. There are contrasting results on
500 this topic: Alfaro et al. (2004) found an excellent correlation between MAE and the iron oxide
501 content, whereas Klaver et al. (2011) found that the single scattering albedo (representing the
502 capacity of an aerosol population to absorb light with respect to extinction) was almost inde-
503 pendent on the mass fraction of iron oxides. Moosmüller et al. (2012) disagreed, pointing out to
504 the uncertainty in the correction procedure of the measurement of absorption by Klaver et al.
505 (2011). As a matter of fact, Klaver et al. (2011) and Alfaro et al. (2004) used the same correction
506 procedure. It is more likely that the lack of correlation found in Klaver et al. (2011) is due to the
507 fact that other minerals than iron oxides contribute to absorption, in particular at their working
508 wavelength (567 nm), where the absorption efficiency of iron oxides starts to weaken. Clearly,
509 the linear correlation between elemental iron in mineral dust and its light-absorption properties
510 could ease the application and validation of climate models that now starting including the rep-
511 resentation of the mineralogy (Perlwitz et al., 2015a; 2015b; Scanza et al., 2015). Also, they
512 would facilitate detecting source regions based on remote sensing of dust absorption in the UV-
513 VIS spectral region (e.g., Hsu et al., 2004). However, such a quantitative relationship cannot
514 uniquely determined from these studies, including the present one, which use different ways of
515 estimating elemental iron, iron oxides and the total dust mass. A more robust estimate should be
516 obtained by estimating the imaginary parts of the complex refractive indices associated to these
517 measurements of absorption, and their dependence on the mineralogical composition.

518 **Author contributions**

519 L. Caponi, P. Formenti, D. Massabò, P. Prati, C. Di Biagio, and J. F. Doussin designed the chamber
520 experiments and discussed the results. L. Caponi and C. Di Biagio realized the experiments with contri-
521 butions by M. Cazaunau, E. Pangui, P. Formenti, and J.F. Doussin. L. Caponi, D. Massabò and P. For-
522 menti performed the full data analysis with contributions by C. Di Biagio, P. Prati and J.F. Doussin. L.
523 Caponi, P. Formenti and S. Chevaillier performed the XRF measurements. P. Formenti and G. Landrot
524 performed the XAS measurements. D. Massabò performed the MWAA and the gravimetric measure-
525 ments. M. O. Andreae, K. Kandler, T. Saeed, S. Piketh, D. Seibert, and E. Williams collected the soil



526 samples used for experiments. L. Caponi, P. Formenti, D. Massabò and P. Prati wrote the manuscript
527 with comments from all co-authors.

528 **Acknowledgements**

529 The RED-DUST project was supported by the French national programme LEFE/INSU, by the EC
530 within the I3 project “Integration of European Simulation Chambers for Investigating Atmospheric Pro-
531 cesses” (EUROCHAMP-2020, grant agreement n. 730997), by the Institut Pierre Simon Laplace (IPSL),
532 and by OSU-EFLUVE (Observatoire des Sciences de l’Univers-Enveloppes Fluides de la Ville à l’Ex-
533 obiologie) through dedicated research funding. C. Di Biagio was supported by the CNRS via the Labex
534 L-IPSL. M. O. Andreae was supported by the Max Society and by King Saud University. The mobility
535 of researchers between Italy and France was supported by the PICS programme MedMex of the CNRS-
536 INSU. The authors acknowledge the CNRS-INSU for supporting CESAM as national facility. K. Kan-
537 dler acknowledges support from the Deutsche Forschungsgemeinschaft (DFG grant KA 2280/2-1).

538 **References**

- 539 Alfaro, S. C., Lafon, S., Rajot, J. L., Formenti, P., Gaudichet, A., and Maille, M., Iron oxides and light
540 absorption by pure desert dust: An experimental study, *J. Geophys. Res. Atmos.*, 109, D08208,
541 doi:10.1029/2003JD004374, 2004.
- 542 Anderson, T. L. and Ogren, J. A., Determining aerosol radiative properties using the TSI 3563 integrat-
543 ing nephelometer, *Aerosol. Sci. Technol.*, 29, 57–69, 1998.
- 544 Andrews, E., Sheridan, P. J., Fiebig, M., McComiskey, A., Ogren, J. A., Arnott, P., Covert, D., Elleman,
545 R., Gasparini, R., Collins, D., Jonsson, H., Schmid, B., and Wang J., Comparison of methods
546 for deriving aerosol asymmetry parameter, *J. Geophys. Res.*, 111, D05S04,
547 doi:10.1029/2004JD005734, 2006.
- 548 Arnott, W., Hamasha, K., Moosmüller, H., Sheridan, P. J., and Ogren, J. A., Towards aerosol light-
549 absorption measurements with a 7-wavelength aethalometer: Evaluation with a photoacoustic
550 instrument and 3-wavelength nephelometer, *Aerosol Sci Tech.*, 39(1), 17–29, 2005.
- 551 Bahadur, R., P. S. Praveen, Y. Xu, and V. Ramanathan, Solar absorption by elemental and brown carbon
552 determined from spectral observations, *PNAS*, 109(43), 17366-17371, 2012.
- 553 Balkanski, Y., Schulz, M., Claquin, T., and Guibert, S., Re-evaluation of Mineral aerosol radiative forc-
554 ing suggests a better agreement with satellite and AERONET data, *Atmos. Chem. Phys.*, 7, 81–
555 95, doi:10.5194/acp-7-81-2007, 2007.
- 556 Bedidi, A., and Cervelle B., Light scattering by spherical particles with hematite and goethitelike optical
557 properties: Effect of water impregnation, *J. Geophys. Res.*, 98(B7), 11941–11952,
558 doi:10.1029/93JB00188, 1993.
- 559 Bond, T.C. and Bergstrom, R.W., Light absorption by carbonaceous particles: an investigative review.
560 *Aerosol Sci. Technol.* 40, 27e67, 2006.



- 561 Boucher, O., Randall, D., Artaxo, P., Bretherton, C., Feingold, G., Forster, P., Kerminen, V.-M., Kondo,
562 Y., Liao, H., Lohmann, U., Rasch, P., Satheesh, S.K., Sherwood, S., Stevens B., and Zhang X.
563 Y., Clouds and Aerosols. In: Climate Change 2013: The Physical Science Basis. Contribution of
564 Working Group I to the Fifth Assessment Report of the Intergovernmental Panel on Climate
565 Change [Stocker, T.F., D. Qin, G.-K. Plattner, M. Tignor, S.K. Allen, J. Boschung, A. Nauels,
566 Y. Xia, V. Bex and P.M. Midgley (eds.)]. Cambridge University Press, Cambridge, United King-
567 dom and New York, NY, USA, 2013.
- 568 Brégonzio-Rozier, L., F. Siekmann, C. Giorio, E. Pangui, S. B. Morales, B. Temime-Roussel, Aline
569 Gratien, V. Michoud, S. Ravier, A. Tapparo, A. Monod, Jean-Francois Doussin, Gaseous prod-
570 ucts and secondary organic aerosol formation during long term oxidation of isoprene and meth-
571 acrolein, Atmos. Chem. Phys., 15, 2953-2968, 2015.
- 572 Brégonzio-Rozier L., C. Giorio, F. Siekmann, E. Pangui, S. B. Morales, B. Temime-Roussel, A. Gratien,
573 V. Michoud, M. Cazaunau, H. L. DeWitt, A. Tapparo, A. Monod and J.-F. Doussin, Secondary
574 Organic Aerosol formation from isoprene photooxidation during cloud condensation-evaporation
575 cycles, Atmospheric Chemistry and Physics, 16: 1747-1760, 2016.
- 576 Bristow, C. S., Hudson-Edwards, K. A., and Chappell, A.: Fertilizing the Amazon and equatorial Atlan-
577 tic with West African dust, Geophys. Res. Lett., 37, L14807, 10.1029/2010GL043486, 2010.
- 578 Buchard, V., da Silva, A. M., Colarco, P. R., Darmenov, A., Randles, C. A., Govindaraju, R., Torres,
579 O., Campbell, J., and Spurr, R.: Using the OMI aerosol index and absorption aerosol optical
580 depth to evaluate the NASA MERRA Aerosol Reanalysis, Atmos. Chem. Phys., 15, 5743–5760,
581 doi:10.5194/acp-15-5743-2015, 2015.
- 582 Chen, L.-W.A., Chow, J.C., Wang, X.L., Robles, J.A., Sumlin, B.J., Lowenthal, D.H., Zimmermann, R.,
583 Watson, J.G., Multi-wavelength optical measurement to enhance thermal/optical analysis for car-
584 bonaceous aerosol, Atmos. Meas. Tech. 8, 451-461, 2015.
- 585 Chen, Y. and Bond, T. C., Light absorption by organic carbon from wood combustion, Atmos. Chem.
586 Phys., 10:1773–1787, 2010.
- 587 Chiapello, I., Dust Observations and Climatology, in P. Knippertz and J.-B.W. Stuut (eds.), Mineral
588 Dust: A Key Player in the Earth System, DOI 10.1007/978-94-017-8978-3__7, ©Springer Sci-
589 enceCBusiness Media, Dordrecht, 2014.
- 590 Chung, C. E., V. Ramanathan, and D. Decremmer, Observationally constrained estimates of carbonaceous
591 aerosol radiative forcing, PNAS, 109(29), 11624-11629, 2012.
- 592 Coakley, J.A. and Chylek, P., The two-stream approximation in radiative transfer: Including the angle
593 of incident radiation, J. Atmos. Sci. 32, 409 – 418, 1975.
- 594 Colarco, P. R., O. B. Toon, O. Torres, and F. J. Rasch, Determining the UV imaginary part of refractive
595 index of Saharan dust particles from TOMS data and a three dimensional model of dust transport,
596 J. Geophys. Res., 107(D16), 10.1029/2001JD000903, 2002.
- 597 Collaud Coen, M., Weingartner, E., Apituley, A., Ceburnis, D., Fierz-Schmidhauser, R., Flentje, H.,
598 Henzing, J.S., Jennings, S.G., Moerman, M., Petzold, A., Schmid, O., Baltensperger, U., Mini-
599 mizing light absorption measurement artifacts of the Aethalometer: evaluation of five correction
600 algorithms, Atmos. Meas. Tech. 3, 457-474, 2010.



- 601 Denjean, C., Paola Formenti, Benedicte Picquet-Varrault, Edouard Pangui, Pascal Zapf, Y. Katrib, C.
602 Giorio, A. Tapparo, A. Monod, B. Temime-Roussel, P. Decorse, C. Mangeney, Jean-Francois
603 Doussin, Relating hygroscopicity and optical properties to chemical composition and structure
604 of secondary organic aerosol particles generated from the ozonolysis of α -pinene, Atmos. Chem.
605 Phys., 15, 3339-3358, 2015a.
- 606 Denjean, C., Paola Formenti, Benedicte Picquet-Varrault, Marie Camredon, Edouard Pangui, Pascal
607 Zapf, Katrib, Y., Giorio, C., Tapparo, A., Temime-Roussel, B., Monod, A., Bernard Aumont,
608 Jean-Francois Doussin, Aging of secondary organic aerosol generated from the ozonolysis of α -
609 pinene: effects of ozone, light and temperature, Atmos. Chem. Phys., 15, 883-897,
610 doi:10.5194/acp-15-883-2015, 2015b.
- 611 Denjean, C., Cassola, F., Mazzino, A., Triquet, S., Chevaillier, S., Grand, N., Bourriane, T., Mom-
612 boisse, G., Sellegri, K., Schwarzenbock, A., Freney, E., Mallet, M., and Formenti, P., Size distri-
613 bution and optical properties of mineral dust aerosols transported in the western Mediterranean,
614 Atmos. Chem. Phys., 15, 21607–21669, doi:10.5194/acpd-15-21607-2015, 2015c.
- 615 Denjean, C., *et al.*, Size distribution and optical properties of African mineral dust after intercontinental
616 transport, J. Geophys. Res. Atmos., 121, 7117–7138, doi:10.1002/2016JD024783, 2016.
- 617 Derimian, Y., A. Karnieli, Y. J. Kaufman, M. O. Andreae, T. W. Andreae, O. Dubovik, W. Maenhaut,
618 and I. Koren: The role of iron and black carbon in aerosol light absorption. Atmos. Chem. Phys.,
619 8, 3623–3637 (2008).
- 620 Di Biagio, C., Formenti P., Styler S. A., Pangui E., and Doussin J.-F., Laboratory chamber measurements
621 of the longwave extinction spectra and complex refractive indices of African and Asian mineral
622 dusts, Geophys. Res. Lett., 41, 6289-6297, doi:10.1002/2014GL060213, 2014.
- 623 Di Biagio, C., Formenti, P., Balkanski, Y., Caponi, L., Cazaunau, M., Pangui, E., Journet, E., Nowak,
624 S., Caquineau, S., Andreae, M. O., Kandler, K., Saeed, T., Piketh, S., Seibert, D., Williams, E.,
625 and Doussin, J.-F.: Global scale variability of the mineral dust longwave refractive index: a new
626 dataset of in situ measurements for climate modelling and remote sensing, Atmos. Chem. Phys.
627 Discuss., doi:10.5194/acp-2016-616, in review, 2016.
- 628 Dubovik, O., B. N. Holben, T. F. Eck, A. Smirnov, Y. J. Kaufman, M. D. King, D. Tanre, and I. Slutsker,
629 Variability of absorption and optical properties of key aerosol types observed in worldwide lo-
630 cations, J. Atmos. Sci., 59, 590–608, 2002.
- 631 Egan, W. G. and Hilgeman, T. W.: Optical Properties of Inhomogeneous Materials: Applications to
632 Geology, Astronomy, Chemistry, and Engineering, Academic Press, 235 pp., 1979.
- 633 Fialho, P., A.D.A. Hansen, R.E. Honrath, Absorption coefficients by aerosols in remote areas: a new
634 approach to decouple dust and black carbon absorption coefficients using seven-wavelength Ae-
635 thalometer data, J. Aeros. Sci., 36, 267–282, 2005.
- 636 Filep, Á., Ajtai, T., Utry, N., Pintér, M., Nyilas, T., Takács, S., Máté, Z., Gelencsér, A., Hoffer, A.,
637 Schnaiter, M., Bozóki, Z., and Szabó, G., Absorption spectrum of ambient aerosol and its corre-
638 lation with size distribution in specific atmospheric conditions after a Red Mud Accident, Aero-
639 sol Air Qual. Res. 13, 49-59, 2013.
- 640 Formenti, P., S. Nava, P. Prati, S. Chevaillier, A. Klaver, S. Lafon, F. Mazzei, G. Calzolari, and M. Chiari,
641 Self-attenuation artifacts and correction factors of light element measurements by X-ray analysis:



- 642 Implication for mineral dust composition studies, *J. Geophys. Res.*, 115, D01203,
643 doi:10.1029/2009JD012701, 2010.
- 644 Formenti, P., Rajot, J. L., Desboeufs, K., Saïd, F., Grand, N., Chevaillier, S., and Schmechtig, C., Air-
645 borne observations of mineral dust over western Africa in the summer Monsoon season: spatial
646 and vertical variability of physico-chemical and optical properties, *Atmos. Chem. Phys.*, 11,
647 6387–6410, doi:10.5194/acp-11-6387-2011, 2011.
- 648 Formenti, P., Caquineau, S., Desboeufs, K., Klaver, A., Chevaillier, S., Journet, E. and Rajot, J. L.,
649 Mapping the physico-chemical properties of mineral dust in western Africa: mineralogical com-
650 position, *Atmos. Chem. Phys.*, 14, 10663–10686, doi:10.5194/acp-14-10663-2014, 2014a.
- 651 Formenti, P., Caquineau, S., Chevaillier, S., Klaver, A., Desboeufs, K., Rajot, J. L., Belin, S. and Briois,
652 V.: Dominance of goethite over hematite in iron oxides of mineral dust from western Africa:
653 quantitative partitioning by X-ray Absorption Spectroscopy, *J. Geophys. Res.*, 2014b.
- 654 Hammer, M. S., Martin, R. V., van Donkelaar, A., Buchard, V., Torres, O., Ridley, D. A., and Spurr, R.
655 J. D.: Interpreting the ultraviolet aerosol index observed with the OMI satellite instrument to
656 understand absorption by organic aerosols: implications for atmospheric oxidation and direct ra-
657 diative effects, *Atmos. Chem. Phys.*, 16, 2507-2523, doi:10.5194/acp-16-2507-2016, 2016.
- 658 Hänel, G., Radiation budget of the boundary layer: Part II. Simultaneous measurement of mean solar
659 volume absorption and extinction coefficients of particles, *Beitr. Phys. Atmos.* 60, 241-247,
660 1987.
- 661 Hänel, G., Optical properties of atmospheric particles: complete parameter sets obtained through polar
662 photometry and an improved inversion technique, *Appl. Opt.* 33, 7187-7199, 1994.
- 663 Harrison, R.M., Beddows, D.C.S., Jones, A.M., Calvo, A., Alves, C., and Pio, C., An evaluation of some
664 issues regarding the use of aethalometers to measure woodsmoke concentrations, *Atmos. Envi-
665 ron.* 80, 540e548, 2013.
- 666 Haywood, J. M., P. N. Francis, M. D. Glew, and J. P. Taylor, Optical properties and direct radiative
667 effect of Saharan dust: A case study of two Saharan outbreaks using data from the U. K. Met.
668 Office C-130, *J. Geophys. Res.*, 106, 18,417–18,430, 2001.
- 669 Haywood, J., Francis, P., Osborne, S., Glew, M., Loeb, N., Highwood, E., Tanr'e, D., Myhre, G., For-
670 menti, P., and Hirst, E., Radiative properties and direct radiative effect of Saharan dust measured
671 by the C-130 aircraft during Saharan Dust Experiment (SHADE). 1: Solar spectrum, *J. Geophys.
672 Res.*, 108(D18), 8577, doi:10.1029/2002JD002687, 2003.
- 673 Hsu, N. C., S.-C. Tsay, M. D. King, and J. R. Herman, Aerosol Properties Over Bright-Reflecting Source
674 Regions, *IEEE Transactions Geos. Remote Sens.*, 42, 557-569, 2004.
- 675 IPCC 2013, Climate Change 2013: The Scientific Basis, Summary for Policymakers, Working Group I
676 Contribution to the Fifth Assessment Report of the Intergovernmental Panel on Climate Change,
677 edited by: Stocker, T. F., Qin, D., Plattner, G.-K., Tignor, M. M. B., Allen, S. K., Boschung, J.,
678 Nauels, A., Xia, Y., Bex, V., Midgley, P. M., Cambridge University Press, Cambridge, UK, 2013.
- 679 Journet, E., Balkanski, Y., and Harrison, S. P., A new data set of soil mineralogy for dust-cycle model-
680 ing, *Atmos. Chem. Phys.*, 14, 3801-3816, doi:10.5194/acp-14-3801-2014, 2014.
- 681 Kandler, K., Benker, N., Bundke, U., Cuevas, E., Ebert, M., Knippertz, P., Rodríguez, S., Schütz, L.,
682 and Weinbruch, S.: Chemical composition and complex refractive index of Saharan Mineral Dust



- 683 at Izaña, Tenerife (Spain) derived by elec-tron microscopy, *Atmos. Environ.*, 41, 8058-8074,
684 10.1016/j.atmosenv.2007.06.047, 2007.
- 685 Kandler, K., Schütz, L., Deutscher, C., Hofmann, H., Jäckel, S., Knippertz, P., Lieke, K., Massling, A.,
686 Schladitz, A., Wein-zierl, B., Zorn, S., Ebert, M., Jaenicke, R., Petzold, A., and Weinbruch, S.,
687 Size distribution, mass concentration, chemical and mineralogical composition, and derived op-
688 tical parameters of the boundary layer aerosol at Tinfou, Morocco, during SAMUM 2006, *Tellus*,
689 61B, 32-50, 10.1111/j.1600-0889.2008.00385.x, 2009.
- 690 Kandler, K., Lieke, K., Benker, N., Emmel, C., Küpper, M., Müller-Ebert, D., Ebert, M., Scheuvs, D.,
691 Schladitz, A., Schütz, L., and Weinbruch, S.: Electron microscopy of particles collected at Praia,
692 Cape Verde, during the Saharan Mineral dust experiment: particle chemistry, shape, mixing state
693 and complex refractive index, *Tellus*, 63B, 475-496, 10.1111/j.1600-0889.2011.00550.x, 2011.
- 694 Karickhoff, S. W. and Bailey, G. W., Optical absorption spectra of clay minerals, *Clays Clay Min.*, 21,
695 59-70, 1973.
- 696 Kirchstetter, T.W., Novakok, T., Hobbs, P.V., Evidence that the spectral dependence of light absorption
697 by aerosols is affected by organic carbon, *J. Geophys. Res.* 109, D21208, 2004.
- 698 Klaver, A., Formenti, P., Caquineau, S., Chevaillier, S., Ausset, P., Calzolari, G., Osborne, S., Johnson,
699 B., Harrison, M., and Dubovik, O., Physico-chemical and optical properties of Sahelian and
700 Saharan mineral dust: in situ measurements during the GERBILS campaign, *Q. J. R. Meteorol.*
701 *Soc.*, DOI:10.1002/qj.889, 2011.
- 702 Knippertz, P., and J.-B. W. Stuut (eds.), *Mineral Dust: A Key Player in the Earth System*, DOI
703 10.1007/978-94-017-8978-3_1, Springer Science+Business Media Dordrecht, 2014.
- 704 Lack, D. A., and Langridge, J. M., On the attribution of black and brown carbon light absorption using
705 the Angström exponent, *Atmos. Chem. Phys.* 13, 10535-10543, 2013.
- 706 Lafon, S., J. Rajot, S. Alfaro, and A. Gaudichet, Quantification of iron oxides in desert aerosol, *Atmos.*
707 *Environ.*, 38, 1211-1218, 2004.
- 708 Lafon, S., Sokolik, I.N., Rajot, J.L., Caquineau, S., Gaudichet, A., Characterization of iron oxides in
709 mineral dust aerosols: Implications for light absorption, *J. Geophys. Res.* 111, D21207,
710 DOI:10.1029/2005JD007016, 2006.
- 711 Laskin, J., Laskin, A., Nizkorodov, S. A., Roach, P., Eckert, P., Gilles, M. K., Wang, B., Lee, H. J., and
712 Hu, Q., Molecular Selectivity of Brown Carbon Chromophores, *Environ. Sci. Technol.*, 48,
713 12047-12055, 2014.
- 714 Lau, K. M., K. M. Kim, Y. C. Sud, and G. K. Walker, A GCM study of the response of the atmospheric
715 water cycle of West Africa and the Atlantic to Saharan dust radiative forcing, *Ann. Geophys.*,
716 27, 4023-4037, doi:10.5194/angeo-27-4023-2009, 2009.
- 717 Lazaro, F. J., L. Gutiérrez, V. Barrón, and M. D. Gelado, The speciation of iron in desert dust collected
718 in Gran Canaria (Canary Islands): Combined chemical, magnetic and optical analysis, *Atmos.*
719 *Environ.*, 42(40), 8987-8996, 2008.
- 720 Lewis, K., Arnott, W. P., Moosmüller, H., Wold, C. E., Strong spectral variation of biomass smoke light
721 absorption and single scattering albedo observed with a novel dual-wavelength photoacoustic
722 instrument, *J. Geophys. Res.* 113, D16203, 2008.



- 723 Liao, H., and Seinfeld, J.H., Radiative forcing by mineral dust aerosols: Sensitivity to key variables, *J.*
724 *Geophys. Res.*, 103, 31,637-31,645, 1998.
- 725 Lide, D. R., CRC Handbook of Chemistry and Physics 1991 – 1992, CRC Press, Boca Raton, Fla., 1992.
- 726 Linke, C., Möhler, O., Veres, A., Mohácsi, A., Bozóki, Z., Szabó, G., and Schnaiter, M., Optical prop-
727 erties and mineralogical composition of different Saharan mineral dust samples: a laboratory
728 study, *Atmos. Chem. Phys.*, 6, 3315–3323, 2006.
- 729 Loeb, N. G., and W. Su, Direct Aerosol Radiative Forcing Uncertainty Based on a Radiative Perturbation
730 Analysis, *J. Climate*, 23, 5288, 2010.
- 731 Massabó, D., Bernardoni, V., Bove, M.C., Brunengo, A., Cuccia, E., Piazzalunga, A., Prati, P., Valli,
732 G., Vecchi, R., A multi-wavelength optical set-up for the characterization of carbonaceous par-
733 ticulate matter, *J. Aerosol Sci.* 60, 34-46, 2013.
- 734 Massabó, D., Caponi, L., Bernardoni, V., Bove, M.C., Brotto, P., Calzolari, G., Cassola, F., Chiari, M.,
735 Fedi, M.E., Fermo, P., Giannoni, M., Lucarelli, F., Nava, S., Piazzalunga, A., Valli, G., Vecchi,
736 R., Prati, P., Multi-wavelength optical determination of black and brown carbon in atmospheric
737 aerosols, *Atmos. Environ.*, 108, 1-12, 2015.
- 738 Massabò, D., Caponi, L., Bove, M.C., Prati, P., Brown carbon and thermal-optical analysis: A correction
739 based on optical multi-wavelength apportionment of atmospheric aerosols, *Atmos. Environ.*,
740 125, 119-125. doi: 10.1016/j.atmosenv.2015.11.011, 2016.
- 741 McConnell, C. L., P. Formenti, E. J. Highwood, and M. A. J. Harrison, Using aircraft measurements to
742 determine the refractive index of Saharan dust during the DODO Experiments, *Atmos. Chem.*
743 *Phys.*, 10(6), 3081-3098, 2010.
- 744 Miller, R.L., Tegen, I. and Perlwitz, J.P., Surface radiative forcing by soil dust aerosols and the hydro-
745 logic cycle, *J. Geophys. Res.*, 109, D04203, doi:10.1029/2003JD004085, 2004.
- 746 Miller, R.L., Knippertz, P., Garcia-Pardo, C.P., Perlwitz, J.P., and Tegen, I., Impact of dust radiative
747 forcing upon climate, *Mineral Dust*, 327-357, Springer Netherlands, 2014.
- 748 Ming, Y., Ramaswamy V, and G. Persad, Two opposing effects of absorbing aerosols on global mean
749 precipitation, *Geophys. Res. Lett.* 37, L13701. doi:10.1029/2010GL042895, 2010.
- 750 Moosmüller, H., Chakrabarty, R. K., and W. P. Arnott, Aerosol light absorption and its measurement:
751 A review, *J. Quant. Spectr. Rad. Trans.*, 110, 844–878, 2009.
- 752 Moosmüller, H., Engelbrecht, J. P., Skiba, M., Frey, G., Chakrabarty, R.K., and Arnott, W.P., Single
753 scattering albedo of fine mineral dust aerosols controlled by iron concentration, *J. Geophys. Res.*,
754 117, D11210, doi:10.1029/2011JD016909, 2012.
- 755 Moskowitz, B. M., R. L. Reynolds, H. L. Goldstein, T. S. Berquó, R. F. Kokaly, and C. S. Bristow, Iron
756 oxide minerals in dust-source sediments from the Bodélé Depression, Chad: Implications for
757 radiative properties and Fe bioavailability of dust plumes from the Sahara, *Aeolian Research*, 22,
758 93-106, 2016.
- 759 Müller, T., Schladitz, A., Massling, A., Kaaden, N., Kandler, K., and Wiedensohler, A., Spectral absorp-
760 tion coefficients and imaginary parts of refractive indices of Saharan dust during SAMUM-1,
761 *Tellus B*, 61, 79–95, doi:10.3402/tellusb.v61i1.16816, 2009.



- 762 Patterson, E. M., D. A. Gillette, and B. H. Stockton, Complex index of refraction between 300 and 700
763 nm for Saharan aerosol, *J. Geophys. Res.*, 82, 3153–3160, 1977.
- 764 Pérez C., S. Nickovic, G. Pejanovic, J. M. Baldasano, and E. Özsoy, Interactive dust-radiation modeling:
765 a step to improve weather forecasts, *J. Geophys. Res.*, 111:D16206.
766 doi:10.1029/2005JD0067172006, 2006.
- 767 Perlwitz J., R. Miller, Cloud cover increase with increasing aerosol absorptivity—a counterexample to
768 the conventional semi-direct aerosol effect, *J. Geophys. Res.*, 115:D08203.
769 doi:10.1029/2009JD012637, 2010.
- 770 Perlwitz, J. P., Pérez García-Pando, C., and R. L. Miller, Predicting the mineral composition of dust
771 aerosols – Part 1: Representing key processes, *Atmos. Chem. Phys.*, 15, 11593-11627,
772 doi:10.5194/acp-15-11593-2015, 2015a.
- 773 Perlwitz, J. P., Pérez García-Pando, C., and R. L. Miller, Predicting the mineral composition of dust
774 aerosols – Part 2: Model evaluation and identification of key processes with observations, *Atmos.*
775 *Chem. Phys.*, 15, 11629-11652, doi:10.5194/acp-15-11629-2015, 2015b.
- 776 Petzold, A., Schönlinner, M., Multi-angle absorption photometry - a new method for the measurement
777 of aerosol light absorption and atmospheric black carbon, *J. Aerosol Sci.* 35, 421-441, 2004.
- 778 Petzold, A., Rasp, K., Weinzierl, B., Esselborn, M., Hamburger, T., Dornbrack, A., Kandler, K., Schütz,
779 L., Knippertz, P., Fiebig, M., Virkkula, A., Saharan dust absorption and refractive index from
780 aircraft-based observations during SAMUM 2006, *Tellus B* 61: 118–130, 2009.
- 781 Petzold, A., Onasch, T., Kebejian, P. and Freedman, A., Intercomparison of a Cavity Attenuated Phase
782 Shift-based extinction monitor (CAPS PMex) with an integrating nephelometer and a filter-based
783 absorption monitor, *Atmos. Meas. Tech.*, 6, 1141–1151, doi:10.5194/amt-6-1141-2013, 2013.
- 784 Ravel, B., and M. Newville, ATHENA, ARTEMIS, HEPHAESTUS: data analysis for X-ray absorption
785 spectroscopy using IFEFFIT, *J. Synchrotron Radiation* 12, 537–541,
786 doi:10.1107/S0909049505012719, 2005.
- 787 Ryder, C. L., Highwood, E. J., Rosenberg, P. D., Trembath, J., Brooke, J. K., Bart, M., Dean, A., Crosier,
788 J., Dorsey, J., Brindley, H., Banks, J., Marsham, J. H., McQuaid, J. B., Sodemann, H., and Wash-
789 ington, R., , Optical properties of Saharan dust aerosol and contribution from the coarse mode as
790 measured during the Fennec 2011 aircraft campaign, *Atmos. Chem. Phys.*, 13, 303-325,
791 doi:10.5194/acp-13-303-2013, 2013a.
- 792 Ryder, C. L., E. J. Highwood, T. M. Lai, H. Sodemann, and J. H. Marsham, Impact of atmospheric
793 transport on the evolution of microphysical and optical properties of Saharan dust, *Geophys. Res.*
794 *Lett.*, 40, 2433–2438, doi:10.1002/grl.50482, 2013b.
- 795 Scanza, R. A., Mahowald, N., Ghan, S., Zender, C. S., Kok, J. F., Liu, X., Zhang, Y., and Albani, S.:
796 Modeling dust as component minerals in the Community Atmosphere Model: development of
797 framework and impact on radiative forcing, *Atmos. Chem. Phys.*, 15, 537–561, doi:10.5194/acp-
798 15-537-2015, 2015.
- 799 Sertsu, S. M., and Sánchez, P. A., Effects of Heating on Some Changes in Soil Properties in Relation to
800 an Ethiopian Land Management Practice, *Soil Sci. Soc. Am. J.*, 42, 940-944, 1978.



- 801 Shen, Z. X., J. J. Cao, R. Arimoto, R. J. Zhang, D. M. Jie, S. X. Liu, and C. S. Zhu, Chemical composition
802 and source characterization of spring aerosol over Horqin sand land in northeastern China, *J.*
803 *Geophys. Res.*, 112, D14315, doi:10.1029/2006JD007991, 2007.
- 804 Sinyuk, A., O. Torres, and O. Dubovik, Combined use of satellite and surface observations to infer the
805 imaginary part of refractive index of Saharan dust, *Geophys. Res. Lett.*, 30(2), 1081,
806 doi:10.1029/2002GL016189, 2003.
- 807 Slingo, A., et al., Observations of the impact of a major Saharan dust storm on the atmospheric radiation
808 balance, *Geophys. Res. Lett.*, 33, L24817, doi:10.1029/2006GL027869, 2006.
- 809 Sokolik, I., and Toon, O., Incorporation of mineralogical composition into models of the radiative prop-
810 erties of mineral aerosol from UV to IR wavelengths, *J. Geophys. Res.*, 104(D8), 9423-9444,
811 1999.
- 812 Solmon, F., Mallet, M., Elguindi, N., Giorgi, F., Zakey, A. and Konaré, A., Dust aerosol impact on
813 regional precipitation over western Africa, mechanisms and sensitivity to absorption properties,
814 *Geophys. Res. Lett.*, 35, L24705, doi:10.1029/2008GL035900, 2008.
- 815 Sun J., Zhang, M., and Liu, T., Spatial and temporal characteristics of dust storms in China and its
816 surrounding regions, 1960-1999: Relations to source area and climate, *J. Geophys. Res.*,
817 106(D10), 10325-10333, 2001.
- 818 Tegen, I. and Lacis, A. A., Modeling of particle size distribution and its influence on the radiative prop-
819 erties of mineral dust aerosol, *J. Geophys. Res.*, doi:10.1029/95JD03610, 1996.
- 820 Torres, O., A. Tanskanen, B. Veihelmann, C. Ahn, R. Braak, P. K. Bhartia, P. Veefkind, and P. Levelt,
821 Aerosols and surface UV products from Ozone Monitoring Instrument observations: An over-
822 view, *J. Geophys. Res.*, 112, D24S47, doi:10.1029/2007JD008809, 2007.
- 823 Utry, N., Ajtai, T., Filep, Á., Pintér, M., Hoffer, A., Bozóki, Z., and Szabó, G., Mass specific optical
824 absorption coefficient of HULIS aerosol measured by a four-wavelength photoacoustic spec-
825 trometer at NIR, VIS and UV wavelengths, *Atmos. Environ.* 69, 321-324, 2013.
- 826 Utry, N., Ajtai, T., Filep, Á., Pintér, M., Tombacz, E., Bozóki, Z., and Szabó, G., Correlations between
827 absorption Ångström exponent (AAE) of wintertime ambient urban aerosol and its physical and
828 chemical properties, *Atmos. Environ.* 91, 52-59, 2014.
- 829 Xian, P., Seasonal migration of the ITCZ and implications for aerosol radiative impact. PhD thesis,
830 Columbia University, 2008.
- 831 Vinoj, V., Rasch, P. J., Wang, H., Yoon, J.-H., Ma. P.-L., Landu, K., and Singh, B., Short-term modu-
832 lation of Indian summer monsoon rainfall by West Asian dust, *Nat. Geosci.*, 7, 308-313,
833 doi:10.1038/ngeo2107, 2014.
- 834 Wang, J., J. F. Doussin, S. Perrier, E. Perraudin, Y. Katrib, E. Pangui, and B. Picquet-Varrault, Design
835 of a new multi-phase experimental simulation chamber for atmospheric photosimulation, aerosol
836 and cloud chemistry research, *Atmos. Meas. Tech.*, 4, 2465-2494, 2011.
- 837 Wang, L., Z. Li, Q. Tian, Y. Ma, F. Zhang, Y. Zhang, D. Li, K. Li, and L. Li, Estimate of aerosol
838 absorbing components of black carbon, brown carbon, and dust from ground-based remote sens-
839 ing data of sun-sky radiometers, *J. Geophys. Res. Atmos.*, 118, 6534-6543,
840 doi:10.1002/jgrd.50356, 2013.



- 841 Weinzierl, B., et al., , Microphysical and optical properties of dust and tropical biomass burning aerosol
842 layers in the Cape Verde region—an overview of the airborne in situ and lidar measurements
843 during SAMUM-2, *Tellus B*, 63(4), 589-618, 2011.
- 844 Yang, M., Howell, S.G., Zhuang, J., Huebert, B.J., Attribution of aerosol light absorption to black car-
845 bon, brown carbon, and dust in China - interpretations of atmospheric measurements during
846 EAST-AIRE, *Atmos. Chem. Phys.* 9, 2035e2050, 2009.
- 847 Zhang, X. Y., Y. Q. Wang, X. C. Zhang, W. Guo, T. Niu, S. L. Gong, Y. Yin, P. Zhao, J. L. Jin, and M.
848 Yu, Aerosol monitoring at multiple locations in China: contributions of EC and dust to aerosol
849 light absorption, *Tellus B*, 60(4), 647-656, 2008.
- 850 Zhao, C., Liu, X., Ruby Leung, L., and Hagos, S.: Radiative impact of mineral dust on monsoon precip-
851 itation variability over West Africa, *Atmos. Chem. Phys.*, 11, 1879-1893, 10.5194/acp-11-1879-
852 2011, 2011.
853

854 **Table captions**

855 **Table 1.** Characteristics of the standards used for the quantification of the iron oxides in the XAS anal-
856 ysis.

857 **Table 2.** Summary of information on the soil samples used in this work.

858 **Table 3.** Chemical characterisation of the dust aerosols in PM_{10.6} and PM_{2.5} (in parentheses) size frac-
859 tions. Columns 3 and 4 report the Si/Al and Fe/Ca elemental ratios obtained from X-Ray Fluorescence
860 analysis. The uncertainty on each individual value is estimated to be 10%. Column 5 reports $MR_{Fe\%}$, the
861 fractional mass of elemental iron with respect to the total dust mass concentration (uncertainty 10%).
862 Column 5 reports $MR_{Fe\%}$, the mass fraction of iron oxides with respect to the total dust mass concentra-
863 tion (uncertainty 15%). For PM_{2.5} the determination of the Si/Al ratio is impossible due to the composi-
864 tion of the filter medium.

865 **Table 4.** Mass absorption efficiency (MAE, $10^{-3} \text{ m}^2 \text{ g}^{-1}$) and Ångström Absorption Exponent (AAE) in
866 the PM_{10.6} and PM_{2.5} size fractions. Absolute errors are in brackets.

867 **Table 5.** Mass absorption efficiency (MAE, $10^{-3} \text{ m}^2 \text{ g}^{-1}$) and Ångström Absorption Exponent (AAE) of
868 literature data discussed in the paper

869

870 **Figure captions**

871 **Figure 1.** Time series of aerosol mass concentration in the chamber for the two companion experiments
872 (Libya sample). Experiment 1 (top panel) was dedicated to the determination of the chemical composi-
873 tion (including iron oxides) by sampling on polycarbonate filters. Experiment 2 (bottom panel) was
874 dedicated to the determination of the absorption optical properties by sampling on quartz filters.

875 **Figure 2.** Location (red star) of the soil and sediment samples used to generate dust aerosols.

876 **Figure 3.** Spectral dependence of the MAE values for the samples investigated in this study in the PM_{10.6}
877 (left) and in the PM_{2.5} (right) mass fractions.

878 **Figure 4.** Illustration of the links between the MAE values and the dust chemical composition found in
879 this study. Left column, from top to bottom: linear regression between MAE values between 375 and
880 850 nm and the fraction of elemental iron with respect to the total dust mass ($MR_{Fe\%}$) in the PM_{10.6}
881 fraction; Middle column: same as left column but respect to the mass fraction of iron oxides to the total



882 dust mass ($MR_{Fe_{ox}\%}$) in the $PM_{10.6}$ size fraction; Right column: same as left column but in the $PM_{2.5}$ size
883 fraction.
884



885 **Table 1.** Characteristics of the standards used for the quantification of the iron oxides in the XAS anal-
886 ysis.

Standard	Stoichiometric Formula	Origin
Illite of Puy	$(\text{Si}_{3.55}\text{Al}_{0.45})(\text{Al}_{1.27}\text{Fe}_{0.36}\text{Mg}_{0.44})\text{O}_{10}(\text{OH})_2(\text{Ca}_{0.01}\text{Na}_{0.01}\text{K}_{0.53}\text{X}(\text{I})_{0.12})$	Puy, France
Goethite	FeO OH	Minnesota
Hematite	Fe_2O_3	Niger
Montmorillonite	$(\text{Na,Ca})_{0.3}(\text{Al,Mg})_2\text{Si}_4\text{O}_{10}(\text{OH})_2 \cdot n(\text{H}_2\text{O})$	Wyoming
Nontronite	$\text{Na}_{0.3}\text{Fe}_2(\text{Si,Al})_4\text{O}_{10}(\text{OH})_2 \cdot n\text{H}_2\text{O}$	Pennsylvania

887

888

889

890 **Table 2.** Geographical information on the soil samples used in this work.

Geographical area	Sample	Desert area	Geographical coordinates
	Morocco	East of Ksar Sahli	31.97°N, 3.28°W
Sahara	Libya	Sebha	27.01°N, 14.50°E
	Algeria	Ti-n-Tekraouit	23.95°N, 5.47°E
Sahel	Mali	Dar el Beida	17.62°N, 4.29°W
	Bodélé	Bodélé depression	17.23°N, 19.03°E
Middle East	Saudi Arabia	Nefud	27.49°N, 41.98°E
	Kuwait	Kuwaiti	29.42°N, 47.69°E
Southern Africa	Namibia	Namib	21.24°S, 14.99°E
Eastern Asia	China	Gobi	39.43°N, 105.67°E
North America	Arizona	Sonoran	33.15 °N, 112.08°W
South America	Patagonia	Patagonia	50.26°S, 71.50°W
Australia	Australia	Strzelecki	31.33°S, 140.33°E

891

892



893 **Table 3.** Chemical characterisation of the dust aerosols in PM_{10.6} and PM_{2.5} (in parentheses) size frac-
 894 tions. Columns 3 and 4 report the Si/Al and Fe/Ca elemental ratios obtained from X-Ray Fluorescence
 895 analysis. The uncertainty on each individual value is estimated to be 10%. Column 5 reports $MR_{Fe\%}$, the
 896 fractional mass of elemental iron with respect to the total dust mass concentration (uncertainty 10%).
 897 Column 5 reports $MR_{Fe\text{-}ox\%}$, the mass fraction of iron oxides with respect to the total dust mass concen-
 898 tration (uncertainty 15%). For PM_{2.5} the determination of the Si/Al ratio is impossible due to the com-
 899 position of the filter medium.
 900

Geographical area	Sample	Si/Al	Fe/Ca	MC _{Fe%}	MC _{Fe-ox%}
Sahara	Morocco	3.12 (---)	0.24 (0.28)	3.6 (4.4)	1.4 (1.8)
	Libya	2.11 (---)	1.19 (1.12)	5.2 (5.6)	3.1 (3.4)
	Algeria	2.51 (---)	3.14 (4.19)	6.6 (5.4)	2.7 (2.2)
Sahel	Mali	3.03 (---)	2.99 (3.67)	6.6 (33.6)	3.7 (18.7)
	Bodélé	5.65 (---)	12.35 (----)	4.1 (----)	0.7 (----)
Middle East	Saudi Arabia	2.95 (---)	0.29 (0.27)	3.8 (5.1)	2.6 (3.5)
	Kuwait	3.15 (---)	0.89 (1.0)	5.0 (13.6)	1.5 (4.2)
Southern Africa	Namibia	3.41 (---)	0.11 (0.10)	2.4 (6.9)	1.1 (3.1)
Eastern Asia	China	2.68 (---)	0.77 (0.71)	5.8 (13.6)	0.9 (2.5)
North America	Arizona	3.30 (---)	0.95 (----)	5.3 (----)	1.5 (----)
South America	Patagonia	4.80 (---)	4.68 (4.64)	5.1 (----)	1.5 (---)
Australia	Australia	2.65 (---)	5.46 (4.86)	7.2 (11.8)	3.6 (5.9)

901

902



903 **Table 4.** Mass absorption efficiency (MAE, $10^{-3} \text{ m}^2 \text{ g}^{-1}$) and Ångström Absorption Exponent (AAE) in
904 the $\text{PM}_{10.6}$ and $\text{PM}_{2.5}$ size fractions. Absolute errors are in brackets.

		$\text{PM}_{10.6}$					
Geographical area	Sample	375 nm	407 nm	532 nm	635 nm	850 nm	AAE
Sahara	Morocco	--- (---)	--- (---)	--- (---)	--- (---)	--- (---)	--- (---)
	Libya	89 (11)	75 (9)	30 (5)	--- (---)	--- (---)	3.2 (0.3)
	Algeria	99 (10)	80 (10)	46 (7)	16 (3)	15 (3)	2.5 (0.3)
Sahel	Mali	--- (---)	103 (18)	46 (12)	--- (---)	--- (---)	--- (---)
	Bodélé	37 (4)	25 (3)	13 (2)	6 (1)	3 (1)	3.3 (0.3)
Middle East	Saudi Arabia	90 (9)	79 (8)	28 (3)	6 (1)	4 (1)	4.1 (0.4)
	Kuwait	--- (---)	--- (---)	--- (---)	--- (---)	--- (---)	2.8 (0.3)
Southern Africa	Namibia	52 (7)	49 (7)	13 (3)	5 (2)	1 (2)	4.7 (0.5)
Eastern Asia	China	65 (8)	58 (7)	32 (4)	8 (2)	7 (2)	3 (0.3)
North America	Arizona	130 (15)	99 (12)	47 (7)	21 (4)	13 (4)	3.1 (0.3)
South America	Patagonia	102 (11)	80 (9)	29 (4)	17 (2)	10 (2)	2.9 (0.3)
Australia	Australia	135 (15)	121 (13)	55 (7)	26 (4)	14 (3)	2.9 (0.3)

905

906



		PM _{2.5}					
Geographical area	Sample	375 nm	407 nm	532 nm	635 nm	850 nm	AAE
Sahara	Morocco	107 (13)	88 (11)	34 (6)	14 (3)	15 (4)	2.6 (0.3)
	Libya	132(17)	103 (14)	33 (7)	--- (---)	--- (---)	4.1 (0.4)
	Algeria	95(8)	71 (11)	37 (7)	12 (5)	12 (5)	2.8 (0.3)
Sahel	Mali	711 (141)	621 (124)	227 (78)	--- (---)	--- (---)	3.4 (0.3)
	Bodelé	--- (---)	--- (---)	--- (---)	--- (---)	--- (---)	--- (---)
Middle East	Saudi Arabia	153 (18)	127 (15)	42 (7)	8 (4)	6 (4)	4.5 (0.5)
	Kuwait	270 (100)	324 (96)	--- (---)	54 (52)	--- (---)	3.4 (0.3)
Southern Africa	Namibia	147 (36)	131 (32)	31 (21)	6 (16)	3 (15)	5.1 (0.5)
Eastern Asia	China	201 (30)	176 (26)	89 (17)	14 (10)	23 (10)	3.2 (0.3)
North America	Arizona	--- (---)	--- (---)	--- (---)	--- (---)	--- (---)	--- (---)
South America	Patagonia	--- (---)	--- (---)	--- (---)	--- (---)	--- (---)	2.9 (0.3)
Australia	Australia	335 (39)	288 (33)	130 (19)	57 (11)	36 (9)	2.9 (0.3)

907
908



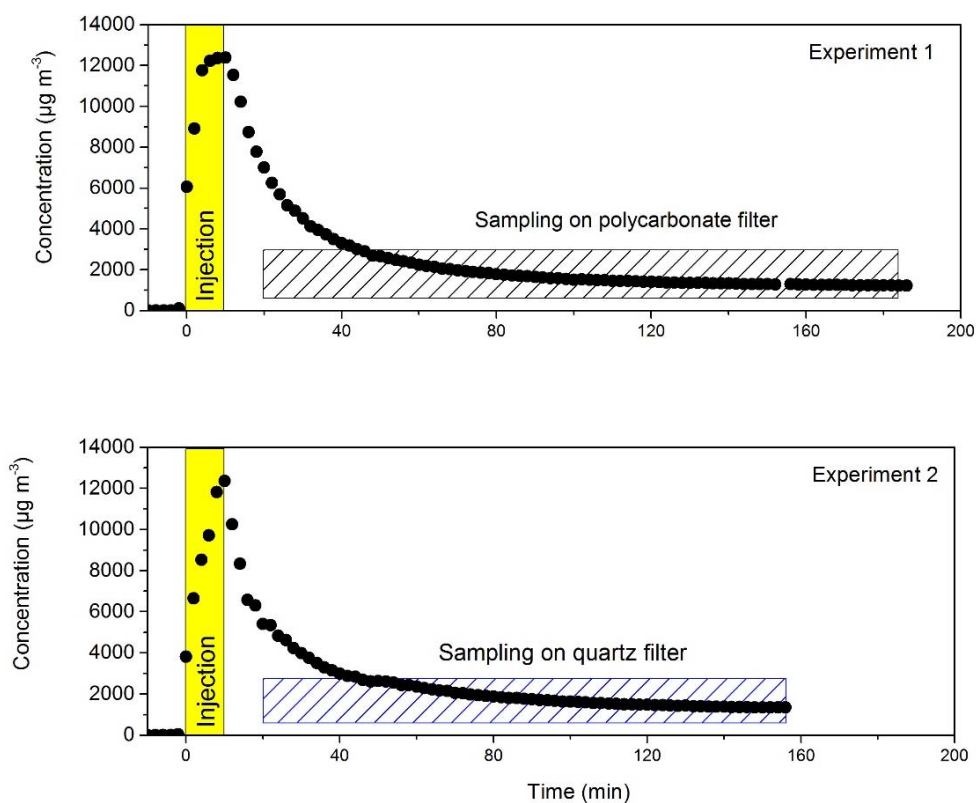
909 **Table 5.** Mass absorption efficiency (MAE, $10^{-3} \text{ m}^2 \text{ g}^{-1}$) and Ångström Absorption Exponent (AAE) of
 910 literature data discussed in the paper

Geo- graph- ical area	Sample	266 nm	325 nm	428 nm	532 nm	660 nm	880 nm	106 4 nm	AAE
	Morocco*								2.25– 5.13
	Morocco, PM _{2.5} [£]								2.0–6.5
Sa- hara	Morocco, submicron [#]	1100			60			30	4.2
	Egypt, submicron [#]	810			20				5.3
	Tunisia [§]		83			11			
	Saharan, transported [¶]								2.9 ± 0.2
	Saharan, transported (PM ₁₀) [%]			37	27 ^{%%}	15 ^{%%%}			2.9
	Saharan, transported (PM ₁) [%]			60	40 ^{%%}	30 ^{%%%}			2.0
Sahel	Niger [§]		124			19			
East- ern Asia	China [§]		69			10			
	China ^{&}		87 ^{&}	50 ^{&&}	27 ^{&&&}	13	1		3.8
Ara- bian Penin- sula, N/NE Af- rica, Cen- tral Asia	Various locations [@]								2.5-3.9

911 * Müller et al. (2008)
 912 [£] Petzold et al. (2008)
 913 [#] Linke et al. (2006)
 914 [§] Alfaro et al. (2004)
 915 [¶] Fialho et al. (2005)
 916 [%] Denjean et al. (2016); ^{%%} at 528 nm, ^{%%%} at 652 nm
 917 [&] Yang et al. (2009); ^{&&} at 375 nm, ^{&&&} at 470 nm, ^{&&&&} at 590 nm
 918 [@] Mossmüller et al. (2012)
 919
 920

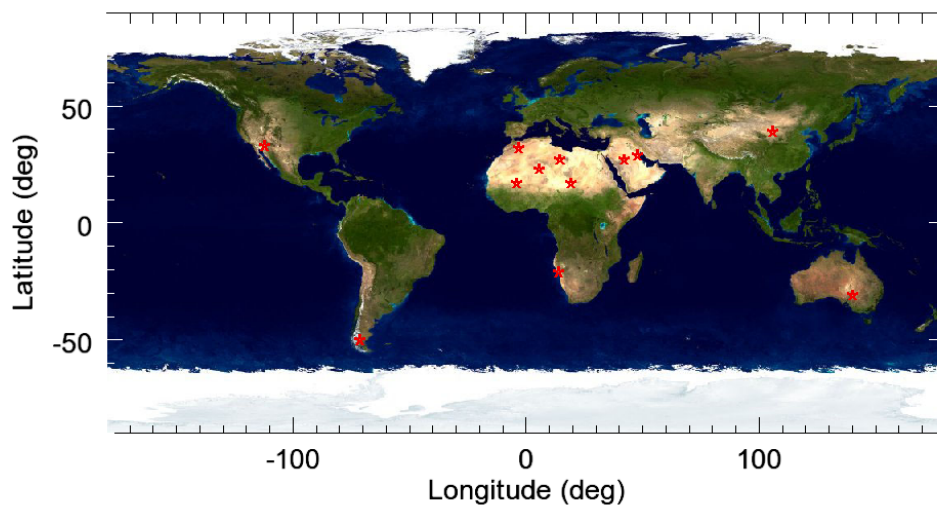


921 **Figure 1.** Time series of aerosol mass concentration in the chamber for the two companion experiments
922 (Libya sample). Experiment 1 (top panel) was dedicated to the determination of the chemical composi-
923 tion (including iron oxides) by sampling on polycarbonate filters. Experiment 2 (bottom panel) was
924 dedicated to the determination of the absorption optical properties by sampling on quartz filters.



925

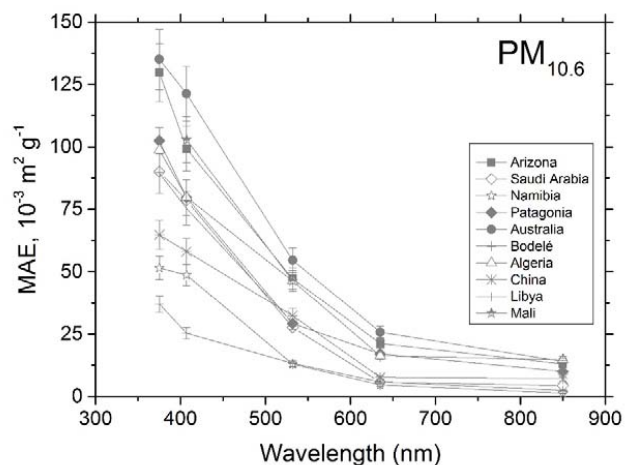
926 **Figure 2.** Location (red star) of the soil and sediment samples used to generate dust aerosols.



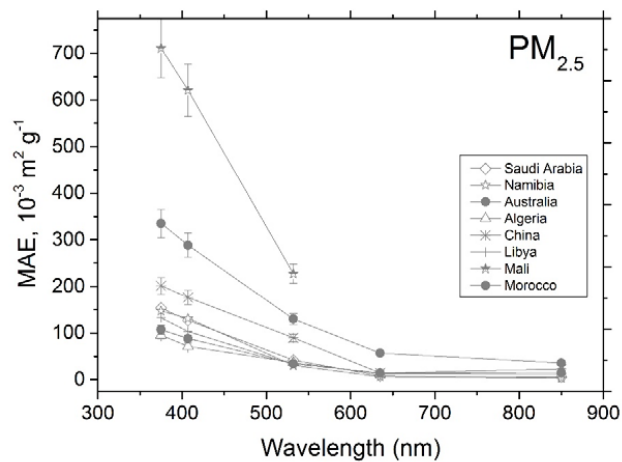
927
928



929 **Figure 3.** Spectral dependence of the MAE values for the samples investigated in this study in the PM_{10.6}
930 (left) and in the PM_{2.5} (right) mass fractions.



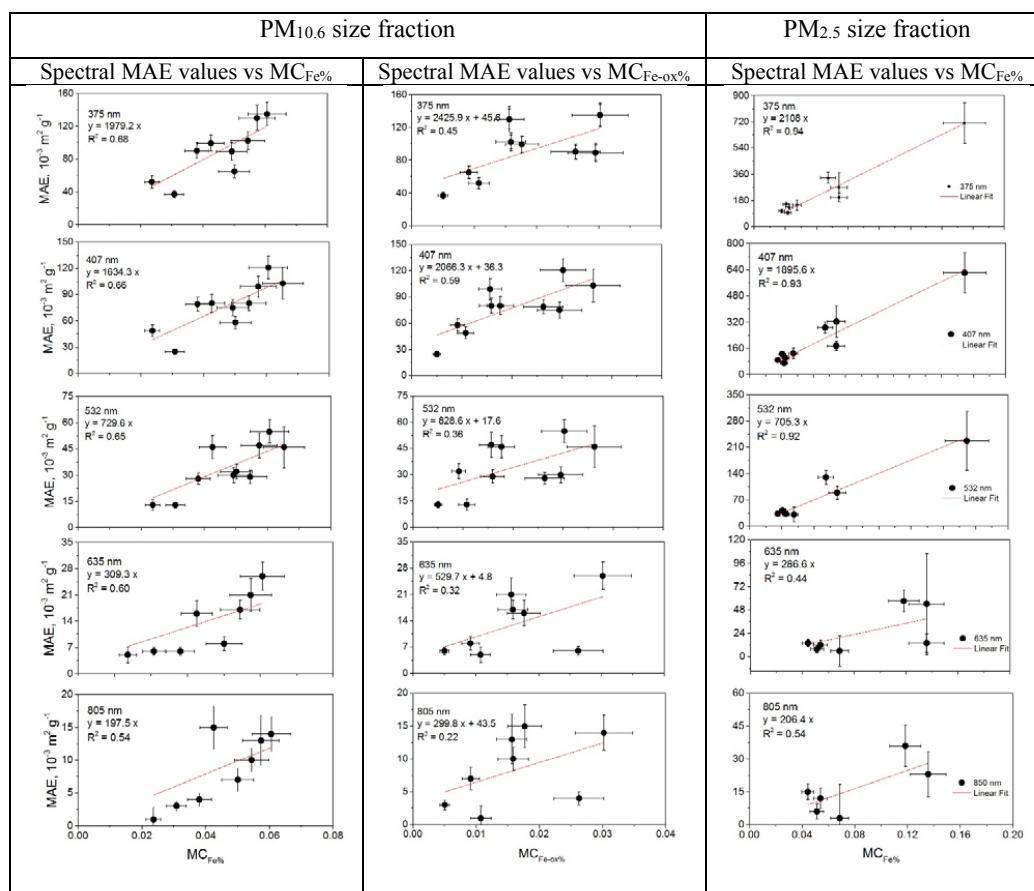
931



932



933 **Figure 4.** Illustration of the links between the MAE values and the dust chemical composition found in
 934 this study. Left column, from top to bottom: MAE values between 375 and 850 nm versus the fraction
 935 of elemental iron with respect to the total dust mass ($MR_{Fe\%}$) in the $PM_{10.6}$ fraction; Middle column:
 936 same as left column but versus the mass fraction of iron oxides to the total dust mass ($MR_{Fe\text{ ox}\%}$) in the
 937 $PM_{10.6}$ size fraction; Right column: same as left column but in the $PM_{2.5}$ size fraction. The linear regres-
 938 sion lines between MAE and $MR_{Fe\%}$ and MAE and $MR_{Fe\text{ ox}\%}$ are reported in each plot.



939
 940